Dutch Buildings Flood Fragility

Masonry Wall Experiments at Flood Proof Holland

Korswagen, Paul A.; Bricker, Jeremy; Diaz-Loaiza, M. Andres

Publication date
2021

Document Version
Final published version

Citation (APA)
Korswagen, P. A., Bricker, J. (Ed.), & Diaz-Loaiza, M. A. (Ed.) (2021). *Dutch Buildings Flood Fragility: Masonry Wall Experiments at Flood Proof Holland*. Delft University of Technology.

TU Delft Delft University of Technology

Project number	C71H14
Report number	C71H14-01
Date	19 of March of 2021
Version	2.1
Status	Final

DUTCH BUILDINGS' FLOOD FRAGILITY

Masonry Wall Experiments at Flood Proof Holland

REPORT

Final

Authors Paul Korswagen

P.A.KorswagenEguren@tudelft.nl

Address Delft University of Technology

Faculty of Civil Engineering and Geosciences

Stevinweg 1, 2628 CN, Delft

TU Delft Delft University of Technology

Faculty of Civil Engineering and Geosciences

Stevinweg 1

2628 CN Delft

PO 5048

2600 GA Delft

www.citg.tudelft.nl

REPORT

Title:

Dutch Buildings Flood Fragility - Masonry Wall Experiments at Flood Proof Holland

Author(s):

Paul Korswagen

Date:

19 of March of 2021

Client(s):	Version:	Status:
TKI Project	2.1	Final

Project number:	Project name:	File reference:
C71H14	Dutch Buildings Flood Fragility	C71H14-01

Cite as:

Korswagen, P. (2021). Dutch Buildings Flood Fragility - Masonry Wall Experiments at Flood Proof Holland. Report number C71H14-01, Report - 19 of March

Document checking			
	Prepared by	Checked by	Approved by
Name	Paul **Korswagen**	Jeremy **Bricker** M. Andrés **Diaz Loaiza**	
Signature	PK	JB, AD	

Revision History

Document		Revision		
Version	Date	Date	Author	Description
1.1	12 October			Draft

TU Delft

I. Summary

To pragmatically answer the question of whether masonry walls can withstand a hydrostatic water pressure, a clay-brick wall was built and tested at Flood Proof Holland. The specimen was exposed to various hydrostatic loads, also in combination with debris impact loads, with the goal of providing experimental data for the calibration of structural models and later development of fragility models to study and assess (economic) damage and life loss from potential Dutch floods.

The 2.7x2.7 m^2 wall, 100 mm thick, was constructed on a steel rig and subjected to a water level difference of up to 125 cm, where the level, at what was considered the back of the wall, was kept low (0 cm). The wall, which was restrained on all four boundaries by being glued at the bottom and top steel beams and constrained against the lateral steel columns of the rig, was subjected to various combinations of water level in front and behind it with the most unfavourable combinations leading to minor cracking. The out-of-plane deformation, perpendicular to the face of the wall, reached approximately 2 mm for the hydrostatic pressure produced by 95 cm of water. The masonry structure, which was also subjected to a vertical overburden by the steel rig mimicking the vertical stress produced by gravity loads on buildings, deformed in two-way bending, meaning that the horizontal supports also prevented the wall from moving.

Non-linear, finite element models calibrated against the experimental results offered additional insight into the behaviour of the wall. It was observed that the wall behaved linear-elastically up to a water level of about 90 cm. At higher water levels, the deformation of wall increased significantly which is associated, according to the models, to the initiation of cracking in the wall and the redistribution of the bending stresses from the vertical (stiffer yet weaker) direction to the stronger horizontal direction. At 125 cm, the wall deformation reached up to 5 mm. From hereon, damage in the wall would have progressed, further reducing its stiffness up until collapse at approximately 150 cm of water depth. This latter value could not be achieved experimentally but is inferred from the trend of the experimental results and the understanding provided from the non-linear models. The models explored comprised analytical and numerical models with linear-elastic and non-linear material models, in one- or two-way bending. The behaviour of the wall up until the initiation of cracking could be predicted well with the simpler, one-way bending analytical or FE linear-elastic models, but more complex, two-way bending models were required to output the same fidelity at higher water levels, with only the non-linear, two-way bending FE model capable of representing the experimental behaviour at the highest water levels.
These calibrated models were also used to predict that, if the wall had not been constrained on its sides and thus only at the top and bottom, more alike walls in buildings will long end walls, it would have failed much earlier, at a water depth of about 90 cm depending on the vertical overburden applied.

These values for water depth consider that no water was present behind the wall. During the test, water did not infiltrate through the wall, with the highest water pressures leading only to wetness at the back of the wall. In reality, the inside of a building may be subjected to a water level because of water entering the building through windows or doors. The lower differences of water level between the front (outside) and back of the masonry are also associated with lower out-of-plane displacements and lower internal bending moments in the wall. However, in terms of hydraulic head, if the head was located higher and closer to the middle of the wall, it was observed to be more detrimental than an identical head where the inside of the building is dry.

The masonry wall was also subjected to a combination of hydrostatic pressure and impact of debris. Two types of debris were considered: a floating tree log representing soft debris, and a suspended steel cube, mimicking hard debris. Impacts of the soft debris of up to 1.8 m/s (90 Joules) did not lead to any additional deformations of the wall, while collisions with the steel cube (up to 180 J) in combination with water depth of about 90 cm, did generate accumulated out-of-plane deformations, visible cracking in a diagonal pattern with leakage of water through the cracks, and ultimately local failure of the masonry.

The experiments conducted herein prove that traditional, single-wythe masonry walls in regular buildings can safely withstand water depths of up to 90 cm when the inside of the building is dry. This corresponds roughly to a hydraulic head of 90 cm when the level inside is low. At larger water depths damage in the

form of cracks is expected and the boundaries of the wall and its overburden become relevant in determining whether the wall has sufficient capacity to avert collapse. For a square wall, restrained on all four boundaries, the maximum water level was determined to be about 150 cm; but, wider walls or walls without lateral supports are much more vulnerable having fewer possibilities to redistribute stresses, especially to the horizontal direction and thus exhibiting more brittle failure after the onset of cracking.

Future work should hence focus on testing the difference between one-way and two-way bending in masonry walls, assessing the effect of leakage through walls with openings, and observing the influence of cavity walls where two walls are built in front of each other with a space in-between, which are common in Dutch buildings, and where water outside and inside the building may exert pressure against the empty cavity. The rate at which such a cavity is filled with water would also provide additional insight into the flood resilience of dutch buildings.

II. Table of Contents

1. Introduction

Within the project to physically determine the fragility of Dutch masonry buildings against flooding events, masonry structures and, specifically, outer masonry walls, play an important role in the flood resilience of a great number of Dutch buildings. To pragmatically answer the question of whether typical flood loads will affect the structural integrity of masonry walls, a specimen wall is constructed and tested under a hydrostatic water pressure. Moreover, this test is to help validate analytical and finite-element structural models predicting the behaviour and capacity of masonry structures. The test, conducted in the large basin of the Flood Proof Holland facility, to the south of the TU Delft campus, in combination with the models explored herein, were configured so as to answer the following questions:

- Does a typical fired-clay masonry wall withstand static water levels in the order of 1 metre?
- What are the out-of-plane deformations of the wall when subjected to various water levels?
- Does water flow through the wall and is there a degradation effect when the masonry is subjected to medium-term water pressure?
- What kind of models are better suited to mimic the behaviour of the wall?
- Which boundaries or effects give the wall a residual capacity?
- How does the wall behave when subjected to debris impact loads such as a floating tree log?

Additionally to the wall, small samples, comprising two compression wallets and six bond-wrench couplets, were constructed to determine the material properties of the masonry. These tests, together with the extensive characterisation of baked-clay masonry performed in previous projects, are to give a thorough picture of the type of masonry present in the wall.

This report presents an extensive description of the experiments and their results starting in chapter 2. Then, chapter 3 explores various model alternatives to represent the wall experiment and includes a discussion of the observations. Finally, chapter 4 gathers the main conclusions of this test.

Figure 1. Masonry wall in steel testing rig with water level at -15cm.

2. Experiments

2.1. Masonry Wall at Flood Proof Holland

2.1.1. Geometry and Material

The masonry wall was constructed on June 15th 2020 by a professional mason who had built many masonry samples tested in the Stevin Laboratory. The fired-clay bricks of 'waalformaat' of 210 mm in length, 50 mm in height and 100 mm in thickness, were laid in a stretcher bond pattern with half overlap and 10 mm joints, resulting in a single-wythe wall 100 mm thick. The wall was built 12 bricks wide (2630 mm approx.) and 44 courses tall (2630 mm approx.). The first and last courses were glued to the boundary steel beams using a two-component epoxy glue, while the lateral sides of the wall were placed dry against the steel columns. The mortar was acquired pre-mixed with a recipe consisting of cement and hydrated lime as cementitious components, and fine sand. The final product had a ratio in weight of approximately 1.3:5.5:1 of cementitious aggregates, sand, and water; however, the water quantity was tuned by the mason on site to compensate for the sunny and windy construction conditions. Hence, two compression wallets (2 bricks wide and 8 courses high) and 6 bond-wrench couplets were constructed to later establish any deviations between the material properties of the masonry built at Flood Proof Holland, and the masonry built in the laboratory (see Figure 8.d). The companion samples were left to harden next to the wall for a period of eight weeks before being taken to the laboratory for testing so that they would resemble the wall properties as much as possible.

Figure 8. Construction process of the wall, including glueing of the last course to the top steel beam (c) and the companion specimens (d).

2.1.2. Testing Setup

The wall was constructed within a steel frame consisting of H profiles 300 mm tall and 300 mm wide with 16 mm flanges, 10 mm webs, and 16 mm end-plates. The profiles were bolted together in such a fashion that the resulting rig was capable of safely withstanding the overturning moment produced by the hydrostatic pressure. Moreover, the frame was designed such that a vertical stress could be applied to the wall by means of a spring which could be tightened to achieve the desired force by measuring the deformation of the spring; see Figure 3.c. This design, however, necessitated a somewhat deformable top support consisting only of four 24mm threaded bars. Nonetheless, since the bulk of the hydrostatic pressure was applied at the base of the wall, this compromise was deemed acceptable. The steel rig was further weighted down using sandbags placed in the voids of the construction so that the frame would become sufficiently safe against the potential sliding caused by the water force. The sides of the wall were also supported by a semi-flexible timber profile consisting of hard wood and bolted to the steel frame; the profile was placed against the masonry and the gaps were filled with an acrylic glue. This support could be unbolted later in the test.

Furthermore, the setup was placed in the corner of the basin since this is the deepest location. To complete an L-shaped box that would allow for a high water level outside and a low water level inside, a dike made with available sandbags was constructed; see Figure 3.b. The core of the dike was lined with a plastic sheet to guarantee its impermeability. Similarly, the outside of the steel frame was covered with interlocking timber panels and the holes in the steel profiles were plugged shut. The small remaining openings, such as on the lateral sides of wall were made watertight using silicone.

The setup was instrumented with three potentiometers (Appendix B) placed against the wall on a separate timber support structure; see Figure 3.a. These sensors measured the out-of-plane deformation of the wall on three locations at a resolution of 1 μm, however temperature variations and the effect of the sun, recorded over multiple days, reduced the resolution to 0.2 mm when considering time-spaced points. Additionally, two pressure sensors (Appendix C) were used to measure the water level in front and behind the wall; these sensors have a resolution of 1 mm of water column height and are unaffected by ambient conditions. All sensors were connected to a PC which was configured to record one data point every minute. Two cameras, set to take a photograph every 20 seconds were located one in front and one behind the wall.

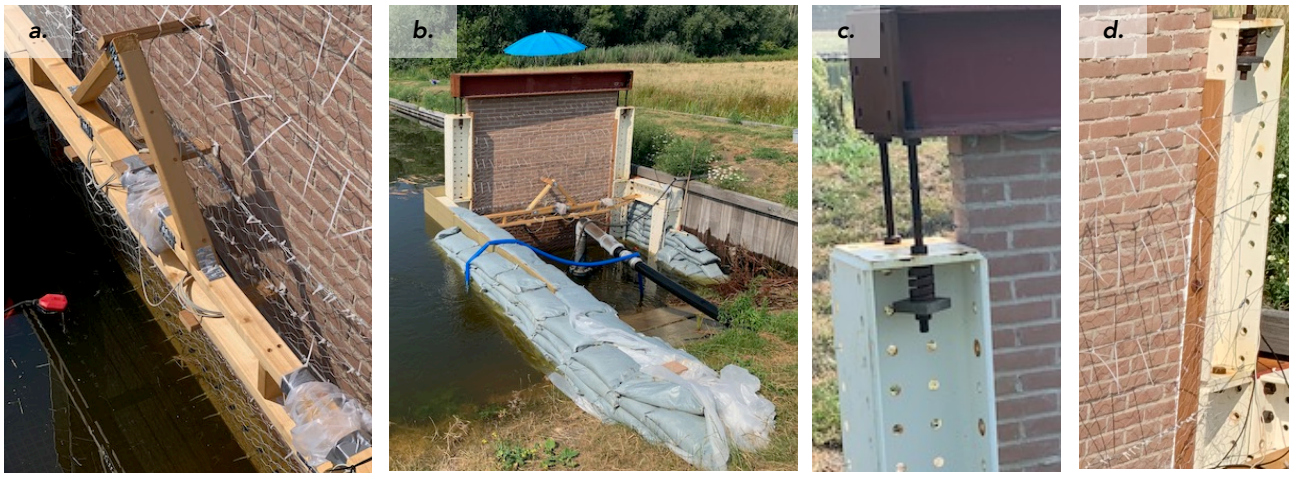

Figure 3. a) Timber support for 3 potentiometers, b) dike made from sand bags, c) spring for application of vertical force on the masonry wall, and d) timber support at the sides.

The water level was controlled by opening the shutter valve from the main basin and allowing the basin to fill with water. Water leaking to behind the wall through the small gaps around the frame was automatically returned to the basin by a small pump; see 'pump 2' on the scheme in Figure 4. If the water level at the backside of the wall became too high, the large pump was engaged to keep the water at the desired level, avoiding the compensation of the hydrostatic pressure from the inside of the wall which would, in most cases, create a less unfavourable situation. A pipe with a plug was also installed to drain the basin at the end of the test.

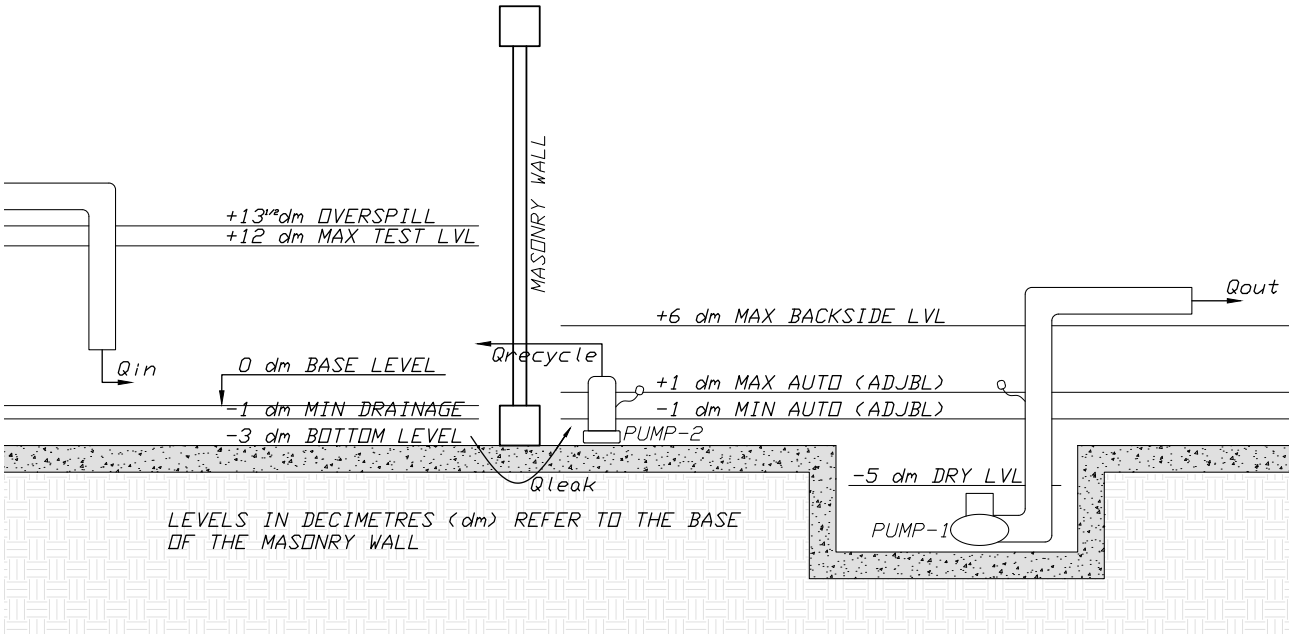

Figure 4. Scheme of water levels.

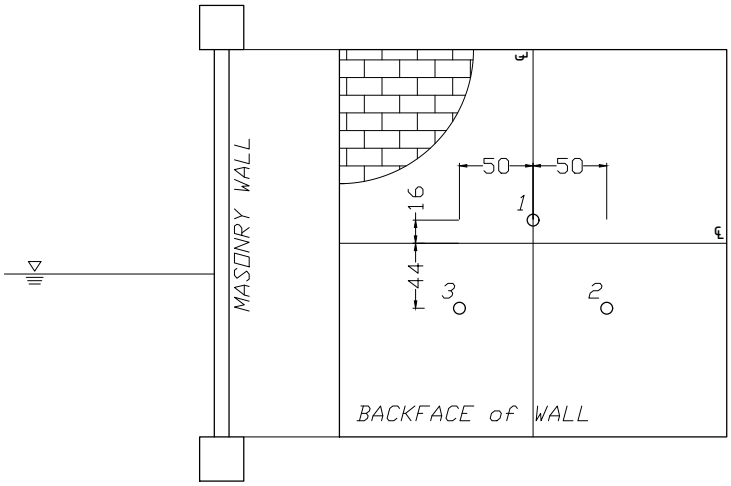

Figure 5. Position of the potentiometers referenced to the centre of the back face of the masonry wall. These sensors measure the out-of-plane displacement, i.e. the displacement perpendicular to the face of the wall.

At the back of the wall, a restraining mesh was secured so as to prevent the catastrophic failure of the wall. Three steel cables of 6 mm in diameter, spanning horizontally the lower middle of the wall, and an additional five cables of a diameter of 3 mm towards the upper middle of the wall, formed the basis of the restraining net anchored to the steel columns on the side of the rig. A 'chicken mesh' of steel wire of 1 mm in diameter was attached to the cables. The restraining mesh was not in contact with the wall and was designed to resist the hydrostatic pressure if the masonry was to slide backwards. In this manner, the pumping equipment and testing rig would be minimally damaged in the event of wall collapse.

2.1.3. Testing Protocol - Hydrostatic Pressure

The wall was subjected to a vertical pre-compression by tightening the springs to a set deformation. Then, a slowly rising water level was used to apply a hydrostatic load on the wall. The water level at the backside was also controlled to produce various loading conditions on the wall. A summary of the five tests performed is presented in Table 1. The precompression was varied between 100 kPa and 10 kPa which corresponds to two normally-loaded timber floors or, for the lower value, to only the self load of the masonry veneer. The maximum water level of 125 cm was determined based on what was achievable in the basin, but corresponded well with the upper boundary of water levels expected during Dutch flooding scenarios.

Table 1. Testing protocol expressed in water levels in dm, vertical pre-compressive stress and duration. See Figure 4.

Test		Description	Water Levels		Duration	Wall Precompression	Pump 1 Levels		Pump 2 Levels	
			Outer	Inner			On	Off	On	Off
1	a	Leakage and Sensor test	3	0	1h	100 kPa	2	0	1	-1
	b	60 cm of water outside	6	0	1h	100 kPa	2	0	1	-1
	c	100 cm / 50 cm	10	5	1h	100 kPa	6	4	1	-1
	d	100 cm - 2 hours	10	0	2h	100 kPa	2	0	1	-1
	e	125 cm / 60 cm	12	6	1h	100 kPa	6	4	1	-1
	f	125 cm / 20 cm	12	2	1h	100 kPa	4	2	1	-1
	g	125 cm - slow drain over 7h	12	0	7h	100 kPa	2	0	1	-1
2	a	80 cm - at lower vertical stress	8	0	1h	50 kPa	2	0	1	-1
	b	90 cm / 60cm	9	6	1h	50 kPa	4	2	1	-1
	c	100 cm	10	0	1h	50 kPa	2	0	1	-1
	d	120 cm / 60 cm	12	6	1h	50 kPa	4	2	1	-1
	e	120 cm	12	0	2h	50 kPa	2	0	1	-1
3	a	80 cm / 60cm	8	6	1h	25 kPa	4	2	1	-1
	b	110 cm - slow drain over 3h	11	0	3h	25 kPa	2	0	1	-1
4	a	80 cm - no timber support	8	0	1h	25 kPa	2	0	1	-1
	b	110 cm - no timber support	11	0	7h	25 kPa	2	0	1	-1
5	a	100 cm - only 10 kPa	10	0	3h	10 kPa	2	0	1	-1

2.1.4. Test Results - Hydrostatic Pressure

The deformation measured by the sensors placed on the wall was captured next to the water levels so as to obtain a relationship between the hydrostatic pressure on the wall and its deformation. Furthermore, the combination of water in front and behind the wall can be observed as an applied bending moment, which offers a clearer relationship to wall deformation. These are depicted in Figure 6. The chronological progress of the test is presented on the horizontal axes and reveals the speed at which the basin was filled and subsequently emptied. As the outer water level rose, a clear deformation was measured by the wall deflectometers; see graphs on the left. This trend is even more evident when the water levels are converted to an equivalent bending moment on the wall, presented in the graphs on the right. Note that the exerted moment is not directly related to the internal bending moment developed in the wall; this is explored later on. The relationship between the outer water level and the deformation of the wall is better illustrated in Figure 7, where the outer water level at times of a near-zero inner water level is plotted against the wall deformation measured by the 3 deflectometers. These graphs also reveal increased wall deformation at high water levels. After the first test, a residual wall deformation is present; this may be linked to permanent damage in the wall or, most likely, an initial deformation of the testing rig as it settles to the lateral loading. The accumulated deformation persists over the test, with one test beginning where the previous ended; the initial point is marked with an 'x'. Note that some tests, like the 1st and 3rd tests, present a horizontal line marking deformation of the sensors at a constant water level. This occurs at high and low water levels, and in both cases, is linked to a long-term presence of the water. At high water levels, this could be attributed to a plastic deformation of the wall, while at lower water levels, the deformation of the sensors is more likely related to temperature, wind or rain effects as the testing setup is left exposed to the environment over night. Consequently, the lower plateaus in Figure 7 should not be disregarded. Additionally, the sensors were reset directly before the fifth test.

In both Figure 6 and Figure 7, the deformation measured by sensor 2 is consistently larger than sensor 3. These two sensors were located at the same height but offset from the centre of the wall; see Figure 5. Figure 7 reveals that even when the sensors were reset for the fifth test, the ultimate deformation of sensor 3 was smaller. This hints at an uneven deformation of the wall on the horizontal plane with the right side of the wall as seen from the front - furthest from the sheet-pile wall and closest to the sandbag dike - deflecting less than the left side. Sensor 1, located at the centre of the wall and thus positioned higher than the other two sensors, shows a smaller deflection than the other two sensors. This is reasonable since the highest deformation of the wall is to be expected around the bottom third where the hydrostatic pressure acts. Moreover, the unloading of the deformation displayed by sensor 1 can also be partly attributed to the elastic deformation of the top of the frame; this phenomenon has a larger influence on sensor 1, since it is placed closer to the top of the frame, and is so reflected by the fact that sensor 1 unloads more than the other two sensors.

Furthermore, the equivalent bending moment applied by the water levels can also be plotted against the wall deformation averaged from the three sensors; this is illustrated in Figure 8. Here, the fifth test is shifted to the end of the fourth test, yet the other values are left untouched. This reveals an increasing, accumulated deformation during the tests, with most of the residual deformation occurring during the first test. Sustained water levels also lead to an increase in deformation. In this light, the rate at which the water level was increased seems to be reflected in the absolute deformation measured. Hence, the stiffness of the indicative force-displacement curve presented in Figure 8 may not be representative of the stiffness of the wall when subjected to the hydrostatic pressure. Nonetheless, comparing the first and fifth test, where the water level was raised much faster for the fifth test, does hint at a reduced stiffness of the wall at the later test. This is summarised in Figure 8, right, where a simple linear fit to the rising branch of the data is made. The lower stiffness of the later test would be attributable to the progressive degradation and damage of the wall.

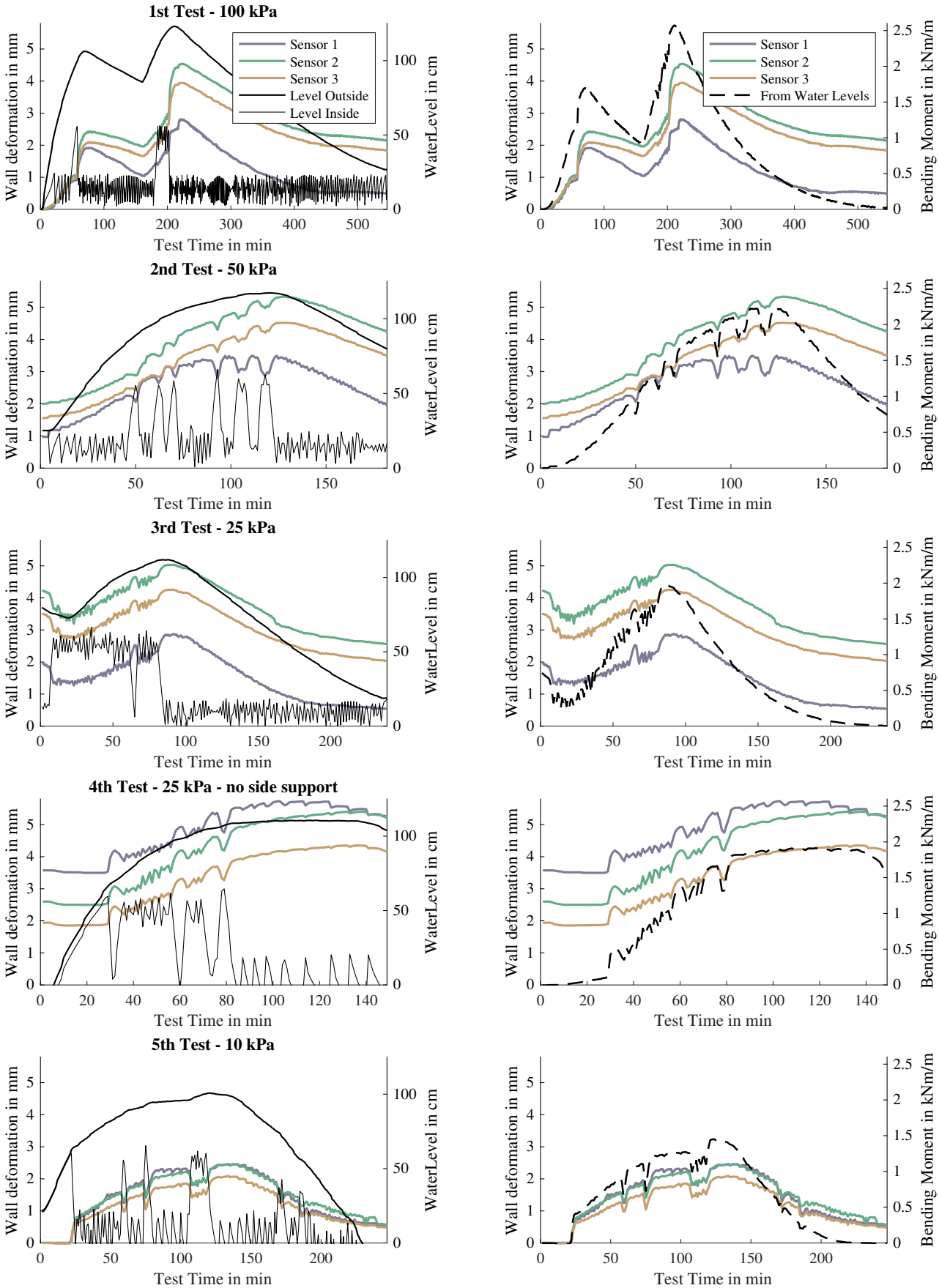

Figure 6. Water levels, sensor deformation, and derived bending moment (from water levels) against test time for the five different tests. The bending moment is derived from the water levels present and is an indication of the severity of the load.

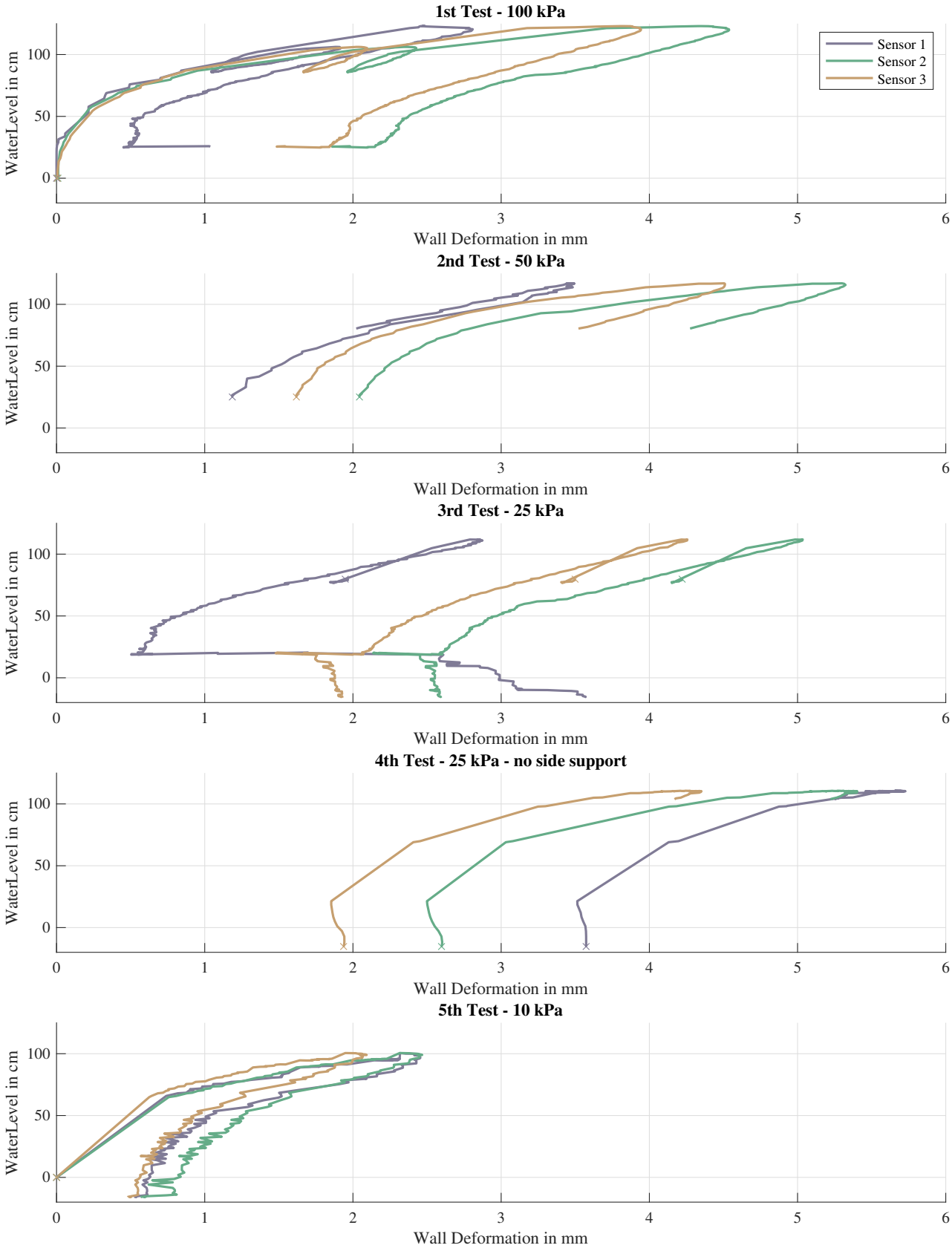

Figure 7. Water level against wall deformation.

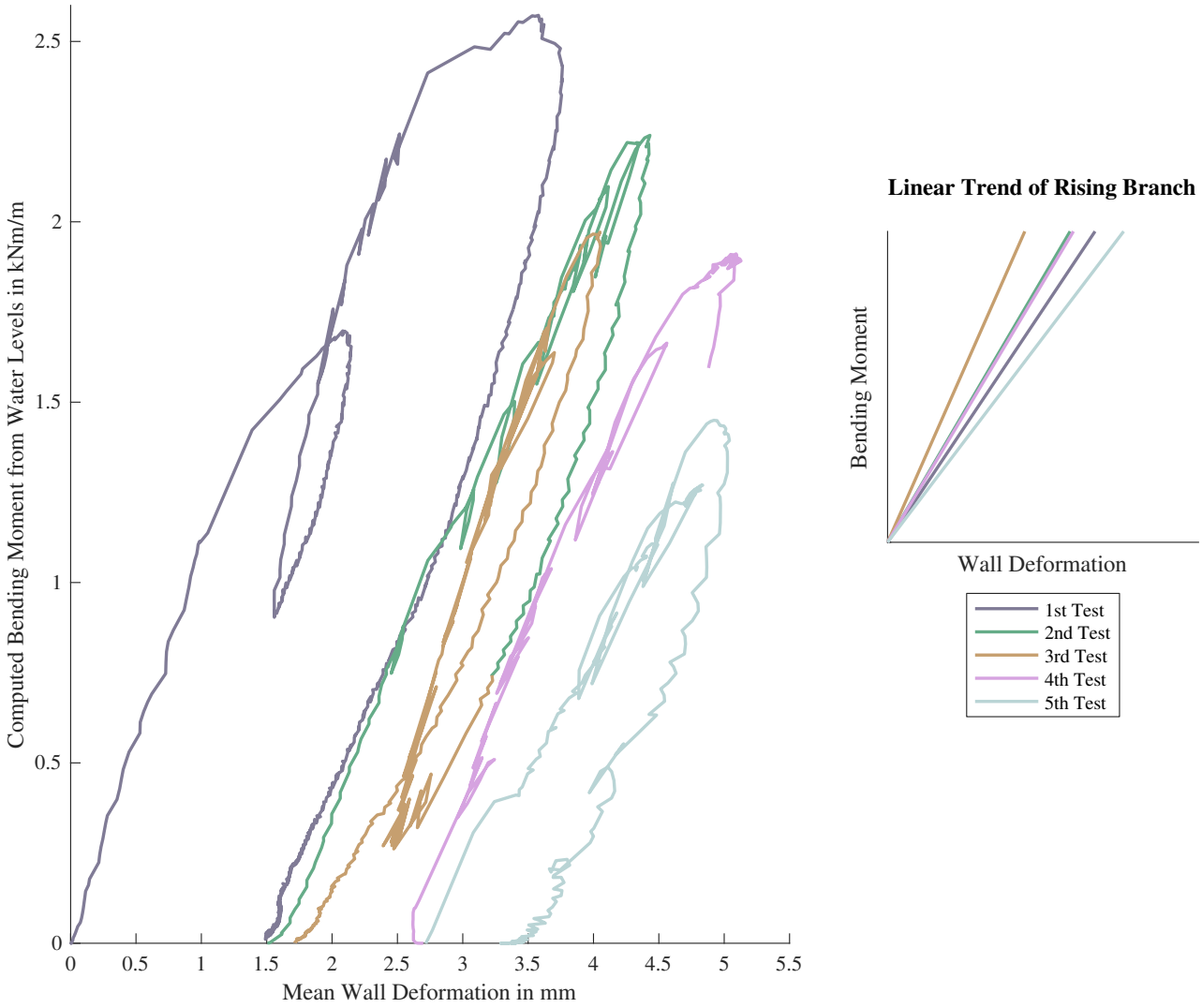

Figure 8. Bending-moment against wall deformation.

2.1.5. Testing Protocol - Debris Experiments

Two types of debris experiments were performed. The first consisted of a floating tree log, about 3 metres in length, 30 cm in diameter and about 80 kg of mass, which was rammed against the wall; see Figure 9. The log was accelerated in the water and given a trajectory perpendicular to the centre of wall; at the moment of impact, the speed of the log was varied between 0.5 and 1.8 m/s over 18 collisions. The wall deformation was measured before and after each impact. The log was to represent "soft" debris floating in flood waters.

Figure 9. Tree log floating in front of the wall.

Secondly, a heavy object, a 30 cm steel cube of 40 kg, was hung from the top of the frame suspended slightly above the water line. This object was to mimic "hard" debris in the water such as cars or metal boats. The object was pulled perpendicularly to the wall and left to swing back to collide with the wall. The potential energy of the object is converted to kinetic energy by the swinging action, which is then absorbed by the wall and the testing rig and transformed into damage or released as dissipating vibrations.

Figure 10. Object swinging against the wall to simulate 'hard' debris.

2.1.6. Test Results - Debris Experiments

Eighteen impact tests were conducted with an increasing speed of the log and at different water levels. Table 2 summarises these tests. The impacts were filmed at 60 frames per second and the velocity of the log was determined by counting the frames required for the log to move the final 10 cm before impact.

While the deformation of the wall during the collision couldn't be recorded accurately, the deformation after each impact can be observed in Figure 11. Here, the water level rises between 90 and 110 cm; two groups of impacts were conducted at a lower (Group 1) and higher (Group 2) water level as depicted by the dotted lines in Figure 11. Here, many of the collisions can be identified by a spike in the wall deformation. This can be contrasted to the middle section of the graphs where no impacts took place and where the rate of increase of the sensor deformation is thus reasonably smooth and only reflects the pump cycles to control the leakage flow. The later impacts, at a higher hydrostatic pressure, led to considerable jumps of up to 0.4 mm in out-of-plane deformation of the wall. Overall, an additional 2 mm of deformation can be attributed to the collisions. This deformation was also not recuperated by the wall when the water was drained.

Table 2. Summary of impacts with a tree log. Left, Group 1 (90 cm), and right, Group 2 (110 cm).

Impact	Speed	Outer Water Level
1	55 cm/s	90 cm
2	75 cm/s	
3	100 cm/s	
4	85 cm/s	
5	85 cm/s	
6	120 cm/s	

Impact	Speed	Outer Water Level
7	85 cm/s	110 cm
8	100 cm/s	
9	85 cm/s	
10	100 cm/s	
11	100 cm/s	
12	75 cm/s	
13	120 cm/s	
14	120 cm/s	
15	100 cm/s	
16	100 cm/s	
17	180 cm/s	
18	150 cm/s	

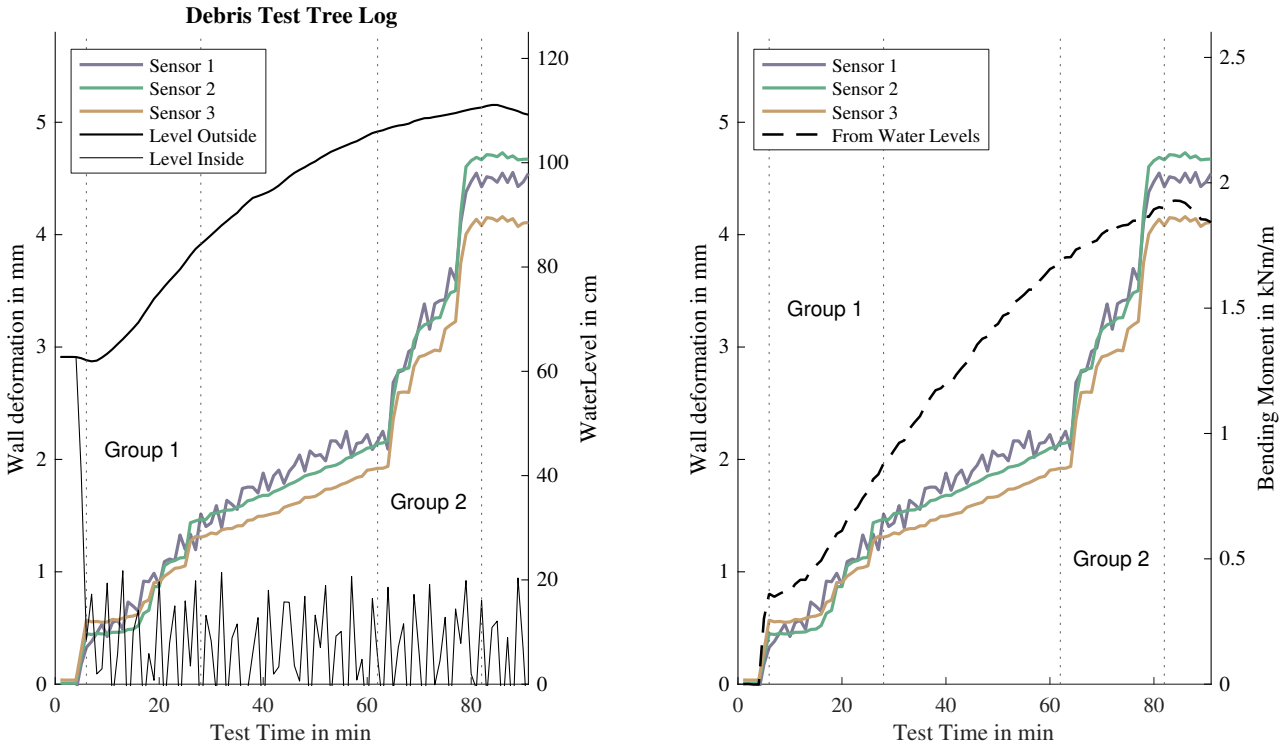

Figure 11. Deformation of the wall after impacts.

Conversely, the steel cube was left to collide with the wall in way similar to that of a wrecking-ball with several dozen repeated collisions on the same location. The energy of the impact was measured from the velocity of the cube and/or its height above the water line when pulled away from the wall. Because the cube hit the same bricks each time, these became damaged and led ultimately to the local failure of the wall. After repeated impacts at a sustained water level of approximately 90 cm in front and no water behind the wall, the wall developed visible diagonal cracks in a staircase pattern which leaked water at some locations; see Figure 13. The cracks, beginning from the centre of the wall, at the location of the impacts, progressed towards the edges of the wall with the largest cracks being present on the lower half of the wall where the water pressure was also acting. This crack pattern resembled the numerical prediction models; see later chapter 3.

The firsts impacts produced strong vibrations which could be felt on the ground when standing several metres away from the testing rig; while the final hits were absorbed by the crushing of the bricks at the impact spot and no vibrations were perceivable.

Figure 12. Left, local damage of the bricks led to a hole in the wall, right. The broken and displaced bricks were trapped by the steel net.

Figure 13. Diagonal stair-like crack pattern from the centre going upwards.

The cube impacts resulted in large deformations measured by the displacement sensors, ultimately reaching and exceeding their measuring range. About 80 min into the test, the majority of the impact energy started to be consumed by the local damage of the bricks which led to a halt of the increase in wall displacement as can be observed in Figure 14. Note also that this is the residual, permanent deformation left by the impact of the debris mimic; the maximum, transitory deformation at the moment of impact was much larger but could not be recorded by the slow sensors. This transitory deformation created small ripples in the water as the wall deformed backwards and bounced back forward.

About 105 hits of varying velocity were necessary to create the hole in the wall seen on Figure 12. The impacts reached up to 3 m/s (as measured from the video frames), with an energy of about 180 Joules. In comparison, the impacts with the log reached only 90 J of energy. Moreover, the stiff steel cube transferred most of the impact energy to the wall while the soft log also dissipated some of the impact energy itself. The energy of the impact was observed to be dissipated by elastic damping of the frame and the wall, hydrodynamic damping due to the displacement of the water with the wall, permanent deformations in the masonry and opening of cracks, and sound.

Instead of the (expected) collapse of the wall, the impact by debris led to local failure of the masonry wall. It is disputable whether a single, stronger impact would have produced collapse or cause a similar local failure.

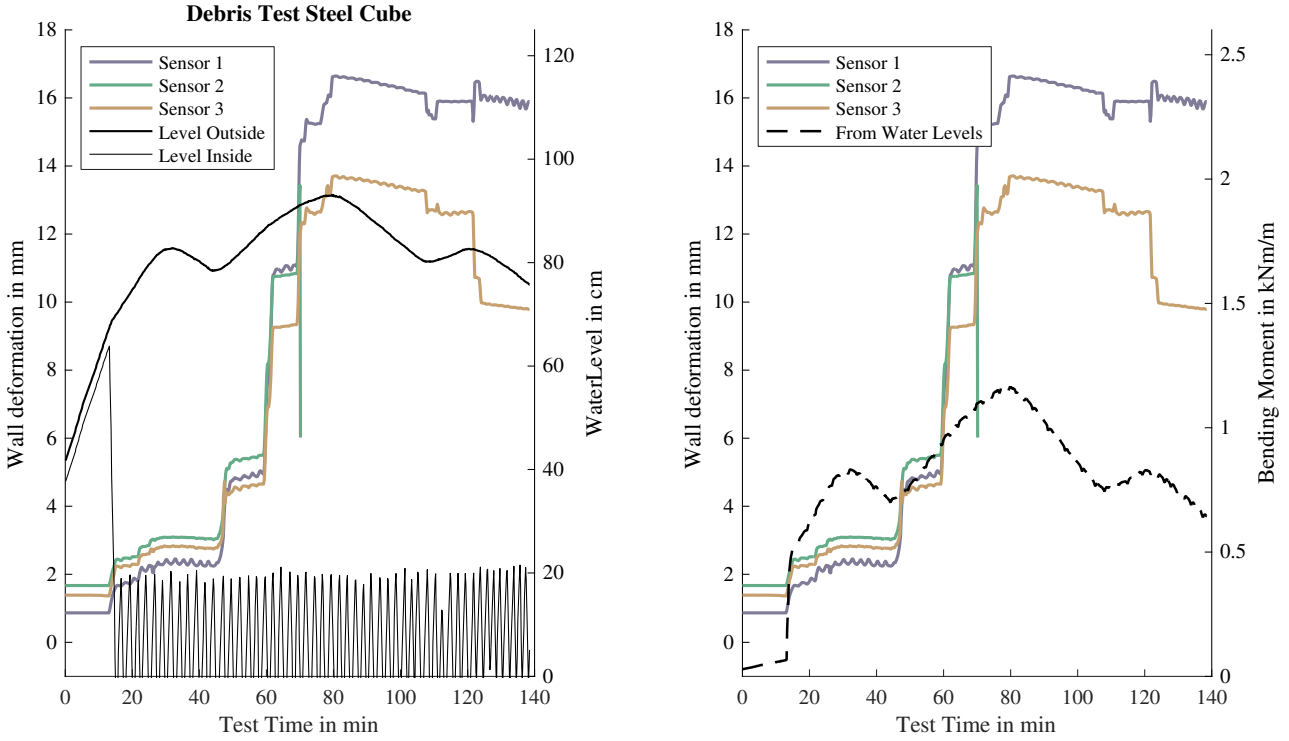

Figure 14. Deformation measured by the out-of-plane deflectometers under relatively-constant water level difference. Note that Sensor 2 dropped out halfway through the test when a large displacement took place.

2.1.7. Leakage and Other Observations

Leakage around the wall and the testing rig is unavoidable and preparations to minimise it were carried out before the experiments. As long as the volume of water leaking to the backside of the wall was significantly smaller than the inflow of water to the basin, leakage would not be a problem. The measures taken to control leakage such as plugging the bolt openings in the steel frame and placing timber boards in front of it, including an impermeable layer in the dike of sandbags, and sealing all the joints with silicone were effective in minimising leakage. However, the gaps between the large concrete plates that make out the floor of the basin were underestimated. These gaps were also sealed underneath the steel frame and around it, but water ended up forcing its way through these gaps by flowing longer distances underneath the plates. This phenomenon, called piping, worsened as the test progressed. In particular, a small concrete tile, located close to the pit of the pump and smaller than the other plates to accommodate the pit, became the outlet of the piping flow; see Figure 15. The sand underneath this tile was carried by the water flow and deposited nearby. Once enough sand had been removed, the tile sunk and the water started flowing underneath the steel frame and over the tile which stopped the transport of sand.

Furthermore, it was interesting to observe that the entire testing rig was slowly displaced by the pressure of the water. The legs of the steel rig were placed about 5 cm from the edge of the slope of the basin made from concrete plates. The sliding stability of the rig was guaranteed by the weight of the additional sandbags; however, the flow underneath the steel rig may have reduced the friction at the bottom of the frame and allowed it to slide until the legs came into contact with the concrete plates. This displacement can be observed in Figure 16 where the original position of the rig can be traced back to the sealant line. Similarly, the side of the frame was bent inwards until the bolted connection was fully activated. This can be observed by the gap formed between the sandbags placed in front of the timbers boards at the side of the rig. The additional weight of the sandbag dike and the lack of underflow on this side of the rig seemed to have prevented it from sliding. These displacements are illustrated in Figure 17.

Figure 15. Small concrete tile (indicated with arrow) and sand scoured from underneath it.

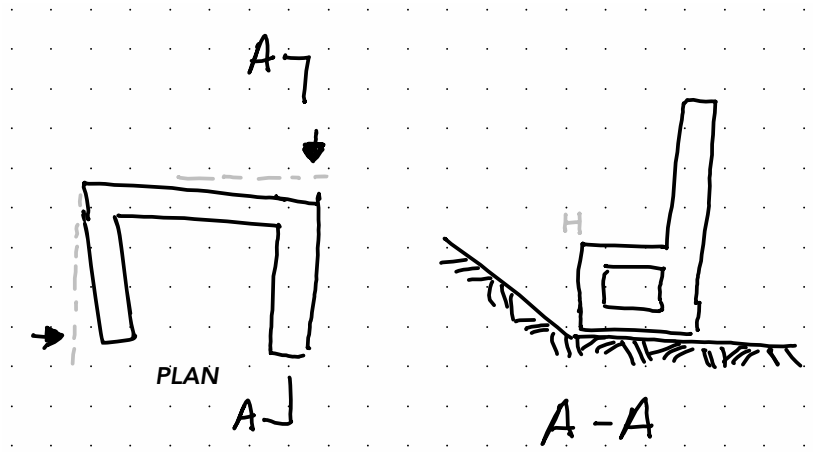

Figure 16. Scheme showing displacements of the frame due to the hydrostatic pressure.

Figure 17. From left to right: gap in the dike, water flowing out of the concrete gaps, and sliding back of the frame.

2.2. Small-Scale Tests

Two types of small-scale tests were performed to characterise the masonry; these are also called companion tests since they should be performed anew for every batch of masonry built. These two tests are not sufficient to give a complete picture of masonry parameters, but provide the most important properties to model out-of-plane bending failure of a masonry wall. Moreover, the properties obtained are compared to similar masonry that has already been extensively characterised in the laboratory. This comparison enables the derivation of properties not directly assayed with the two characterisation tests presented herein.

Six bond-wrench couplets and two compression wallets were constructed at the same time and employing the same mortar batch as the wall. The specimens were left to harden next to the wall for about eight weeks before being taken to the laboratory for testing; see Figure 8.d.

2.2.1. Bond-Wrench Test

The bond-wrench test is a standard test for masonry where the tensile strength of the masonry is inferred from the bond strength between bricks provided by the mortar joint. The direct tensile strength is difficult to measure due to the brittle nature of masonry. The bond strength can be used to determine the tensile strength in the vertical direction (f_{t1}). The tensile strength in the horizontal direction cannot be obtained from this test; an additional shear test would be required to infer the tensile strength in the horizontal direction. However, a relationship between the direct tensile strength and the flexural strength in the vertical direction is known for various masonry types. Moreover, there is also a relationship between the vertical and horizontal flexural strength. The link between the bond strength and the flexural strength in the vertical direction (f_{x1}) is effective in helping to calculate the out-of-plane bending capacity of a masonry wall.

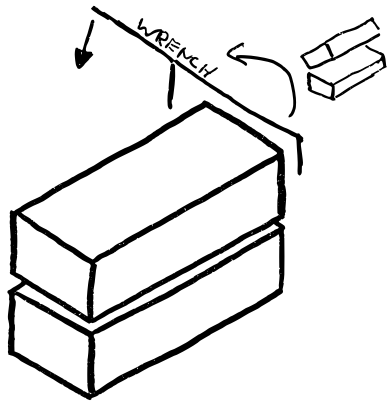

Figure 18. Sketch of a bond-wrench test on a masonry couplet.

The test consists of the application of a bending moment to the top brick of the couplet while the bottom brick is restrained. The bending moment is oriented such that the bricks separate as the mortar joint opens on the longitudinal face; see Figure 18. The bending moment applied is measured and the stress at the joint is computed. The force can be applied manually or by a computer-controlled hydraulic jack; in the latter case, the rate at which the joint opens is measured by a sensor placed between both bricks and is kept constant throughout the test. This also allows to compute the tensile fracture energy.

2.2.2. Compression Wallet Test

The test on a compression wallet is also a standard test used to characterise masonry. The tests outputs the compressive strength of masonry, the Young's modulus of elasticity and the compressive fracture energy. Depending on the direction that the wallet is assayed, either the vertical or horizontal directions can be characterised. For this experiment, both wallets are tested vertically since this is the more relevant direction and some redundancy is needed from the characterisation tests. For this report, the Young's modulus of elasticity in the vertical direction is important. Nonetheless, the compressive strength can also be used to compare and relate different types of masonry.

Different sizes are prescribed for the masonry wallet by various guidelines. The single-wythe wallet eight courses high and two courses wide has become the standard for the 'waalformaat' brick size and is thus comparable to the masonry already assayed in the lab. The wallet is placed on top of a rigid plate that is moved upwards by a hydraulically-operated jack against a rigid top plate. This produces a compressive stress in the masonry. The compressive strain is increased at a constant rate until a peak in the applied force is evident; this corresponds to the compressive strength of the masonry. The stress-strain relationship is then employed to compute the Young's modulus of the material. The test can be continued until the specimen fails in crushing; the total energy employed to reach failure is used to calculate the compressive fracture energy of the masonry.

Figure 19. Wallet for a compression test in the testing rig. The front face of the wallet appears painted for monitoring with photogrammetry.

2.2.3. Experimentally-Determined Material Properties

The experimental results of both tests are collected in Table 3 below. While the compression tests provided expected results, the bond-wrench couplets were too fragile which rendered many tests invalid. Moreover, from the nine initial samples, only six arrived satisfactorily in the lab, and only one provided good results. It is possible that the location of hardening of the samples, albeit next to the wall but perhaps too harshly exposed to the weather, made the small couplets extremely weak. During the demolition of the wall, undamaged parts of the wall did not seem overly fragile and appeared more in-line with the results of the one successful test. Nonetheless, given the high variability usually obtained when assessing the tensile strength of masonry, one test seems insufficient to accurately characterise the masonry of the wall.

Table 3.a. Properties determined from the companion tests.

Bond-Wrench

#	Bond strength MPa	Tensile fracture energy N/m
	f_w	G_{ft}
1	0.01	NA
2	0.01	NA
3	0	NA
4	0.28	20
5	0.01	NA
6	0	NA
CoV	174%	NA
Mean	0.0775	20

Compression Wallet

#	Young's Modulus (vertical) MPa	Compression strength MPa	Compressive fracture energy N/m
	E	f_c	G_{fc}
1	2433	12.8	27
2	2204	11.7	23
CoV	7.0%	6.3%	11.3%
Mean	2318.5	12.25	25

2.2.4. Derived Properties

Using the properties tested and comparing the built masonry to masonry previously and more comprehensively characterised, allows an estimation of additional material parameters. In terms of compression-related properties, the new masonry seems well comparable with similar compressive strength and fracture energy, both at mean value as well as its variability. In this light, the elastic properties could be safely assumed to be similar; this is indicated with an almost equal (≈) sign in Table 3.b. Moreover, since the compressive strength is heavily dependent on the properties of the mortar and the bricks, and the bricks employed were identical, even from the same batch, to previously tested masonry, it can be further extrapolated that the mortar properties of the newer masonry are also comparable to earlier campaigns. In terms of tension-related properties, the mean bond strength is the same as earlier campaigns, however, this is an artifice of the few values tested which can be deducted from the extremely high variability of these tests. It is not possible to say whether the only successfully tested specimen was an outlier value or a representative value. If the latter, then the new masonry would seem to be stronger; yet, this notion is challenged by the large number of fragile specimens. Since this comparison is inconclusive, the bending properties, related to the tensile properties, and the shear properties, related to both compressive and tensile characteristics, remain uncertain.

The bending properties are important when analysing the out-of-plane behaviour of the wall. From these earlier campaigns, it is known that the vertical and in-plane bending (f_{x1} and f_{x3}) are about 2 times higher

than the tensile strength of the masonry. Then, the horizontal bending strength (f_{x2}) is about 1.5 times the vertical bending strength for stretcher-bond masonry. Even though the bond-wrench tests produced inconclusive results, these values need to be determined. Assuming that the new masonry was slightly stronger than the comparison masonry, yet not as strong as the potential outlier value, the bond-strength is estimated at 0.15 MPa. Then, the vertical flexural strength is 0.3 MPa and the horizontal flexural strength is 0.5 MPa. Sensitivity studies on the influence of these values are conducted later in section 3.

Table 3.b. Summary of material properties for characterised clay-brick masonry.

Property		Units	Campaign 2017		Campaign 2018		This experiment (2020)	
			Average	C.o.V.	Average	C.o.V.	Average	C.o.V.
Compressive strength of mortar	f_m	MPa	3.84	0.11	3.59	0.09	≈	
Flexural strength of mortar	f_{mt}	MPa	1.57	0.07	1.55	0.10	≈	
Compressive strength of masonry in the direction perpendicular to bed joints	f'_m	MPa	11.35	0.07	12.93	0.07	12.25	0.06
Elastic modulus of masonry in the direction perpendicular to bed joints	E_1	MPa	2919	0.15	3206	0.25	≈	
	E_2	MPa	2731	0.27	3265	0.29	≈	
	E_3	MPa	3087	0.10	3190	0.24	≈	
Poisson ratio of masonry in the direction perpendicular to bed joints	ν	-	0.14	0.03	0.16	0.35	≈	
Fracture energy in compression for loading perpendicular to bed joints	G_{f-c}	N/m	26.05	0.12	28.63	0.11	25.00	0.11
Masonry bending strength with the moment vector orthogonal to the plane of the wall	f_{x3}	MPa	0.35	0.40			?	
Youngs modulus from IP bending	E_{fx3}	MPa	2084	0.25			?	
Flexural bond strength	f_w	MPa	0.09	0.35	0.08	0.32	0.08	1.74
Fracture energy in tension from bond-wrench test	G_{f-t}	N/m			10	0.50	20	NO
Masonry (bed joint) initial shear strength	f_{v0}	MPa	0.14		0.13	0.30	?	
Masonry (bed joint) shear friction coefficient	μ		0.79		0.82	0.05	?	
Residual masonry (bed joint) initial shear strength	$f_{v0,res}$	MPa	0.03		0.04		?	
Residual masonry (bed joint) shear friction coefficient	$\mu_{\rho\varepsilon\sigma}$		0.71		0.63		?	

3. Comparison to Models

The simplest analytical model of the wall (see section 3.1) would suggest that the wall fails at 80 cm of hydrostatic pressure and 100 kPa of vertical overburden. However, it has been proven that the masonry wall could withstand much deeper water levels and at a much lower beneficial overburden. It is clear that several effects not considered in such a conservative model are contributing to the wall's higher capacity and resilience. For example, the stiffness of the boundaries and the contribution of the lateral boundaries, as well as cracking of the masonry and the redistribution of stresses leading from it, are important effects that are not considered in a one-dimensional model. Moreover, other effects, caused by the nature of the testing rig and its conditions, need also be considered when modelling experimental results; these can prove determinant in the outcome of the model.

The deformation of the wall observed during the tests suggest that the wall would have failed at 145 cm of hydrostatic pressure, a level that could not have been reached in the test. However, the calibrated model also suggests that the wall should have failed when its lateral boundaries were removed already at 95cm, meaning that the removal of these boundaries was not successful and is something that could be improved in future tests. An overview of the models and their comparison to the experiment is summarised in Table 4 next and is discussed over the following sections.

Table 4. Summary of comparison models. See following subsections for details. n.a. = not applicable.

Property	Model A	Model B	Model C	Model D
Type	Analytical	FEM	NL-FEM	NL-FEM
Bending	one-way	two-way	one-way	two-way
Non-linear masonry	No		Yes	
Vertical overburden	50 kPa			
Basic Properties	$E = 5$ GPa; $\nu = 0.15$; $\rho = 1800$ kg/m^3			
Top and bottom rotational stiffness	250 kN/rad			
Lateral interface stiffness	n.a.	35 MN/m^3	n.a.	35 MN/m^3
Masonry strength	$f_{x1} = 0.3$ MPa; $f_{x2} = 0.5$ MPa		$f_t = 0.15$ MPa; $G_f = 40$ Nm/m^2	
Failure criterion	Bending moment	Bending moment	Displacement	Displacement
Failure water level	80 cm	90 cm or 150 cm	95 cm	145 cm

3.1. Analytical Model (A)

The deflection and stress on the wall can be analysed with an analytical model. Model A considers the wall as a slender structure with Euler-Bernoulli bending. Figure 20 illustrates the wall partitioned into a bottom section (a), where the hydrostatic pressure is acting, and a top section (b), where no solicitations are present; the model is presented horizontally for convenience. The analytical model also considers a certain rotational stiffness provided by the bottom and top steel beams, denoted k_a and k_c, respectively. The hydrostatic pressure, depending on the depth of the water (a) is dependent on the x coordinate with origin at the base of the wall. The deflection or out-of-plane deformation of the model is characterised with w(x) for the bottom section and v(x) for the top portion.

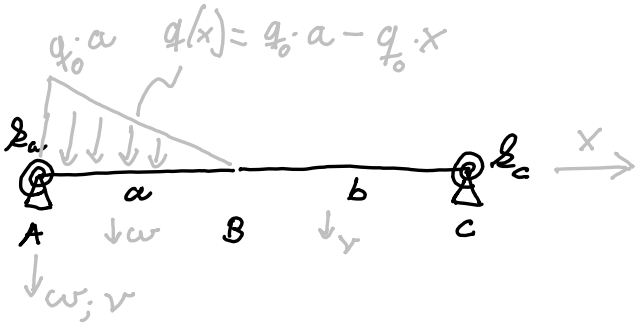

Figure 20. Analytical model for the wall where 'x' is the distance from the bottom of the wall to its height.

This analytical model can be quickly solved by expressing the load on the wall as a function of x and determining its fourth-grade integral which corresponds to the deflection w. This integration process produces four integration constants which have to be computed based on the kinematic and compatibility boundaries of the model. In this case, due to the two portions of the model, eight constants are produced; four of these are determined using the continuity of the wall at point B, where deflection, rotation, bending moment, and shear force are equal; while the remaining four correspond to the zero displacement at both supports and the relationship between the angle and bending moment at the supports. The solution is detailed in appendix B and the resulting graph is presented in Figure 21.

It can be observed how the maximum deflection doesn't occur at the centre height of the wall but is slightly offset towards the bottom; this is due to the hydrostatic pressure which is only applied on the bottom portion of the wall and is greatest at the very bottom. For 100 cm of hydrostatic pressure, the model predicts a maximum deflection of 1.8 mm and bending moment of 600 Nm/m. With the rotational stiffness of the supports, the negative and positive bending moments are similar. Also, the rotational angle at the support is far from zero, suggesting that the rotational stiffness included is not sufficient to provide a perfect double-clamped condition. The model, expressed symbolically, can be evaluated using zero rotational stiffness which leads to an unrealistic deflection of 4.4mm. Then, at infinite stiffness, the deflection decreases to 0.65mm. The stiffness chosen is that of the web of the steel beam when a moment is applied at its top and its bottom is perfectly fixed to the bottom flange; it seems, when comparing the deflection of the model and the experimental values, that the rotational stiffness so selected is well fitting as a rotational constraint. Moreover, the similar positive and negative bending moments that result from this configuration are efficient in the sense that the wall is capable of remaining in the linear-elastic regime without one of the two locations failing first. This gave, unknowingly, a higher LE capacity to the wall.

Furthermore, Figure 22 depicts the situation of an increasing water depth in front of the wall; the vertical line, at 95 cm, marks the point at which the bending moment exceeds the strength of the wall. Of course, the linear-elastic analytical model does not consider this effect. Later, in section 3.4, a comparison to the experimental values is made. Finally, Figure 23 presents a similar picture but including the deflection of the wall over its entire height.

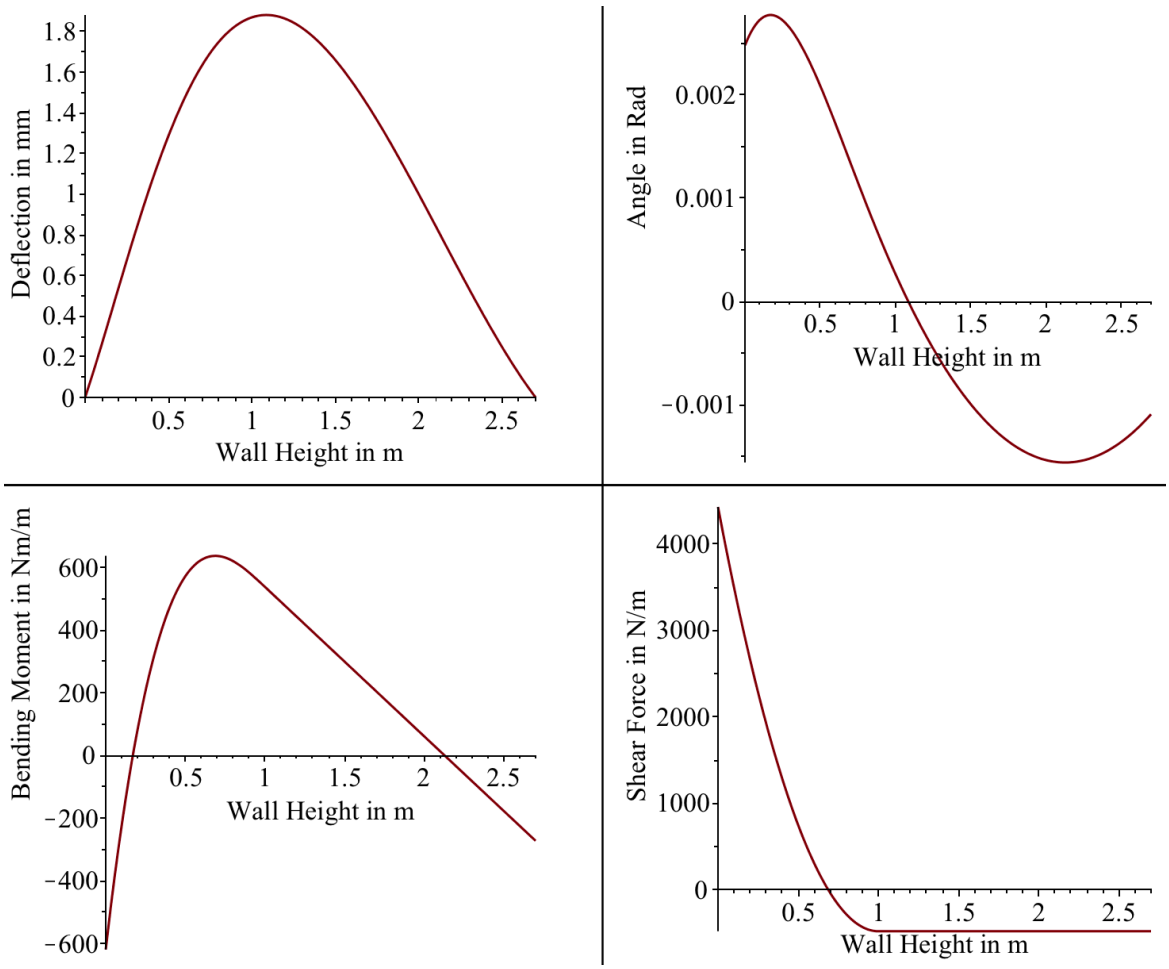

Figure 21. Deflection, line rotation, bending moment and shear force against wall height for a water depth of 1m (a=1).

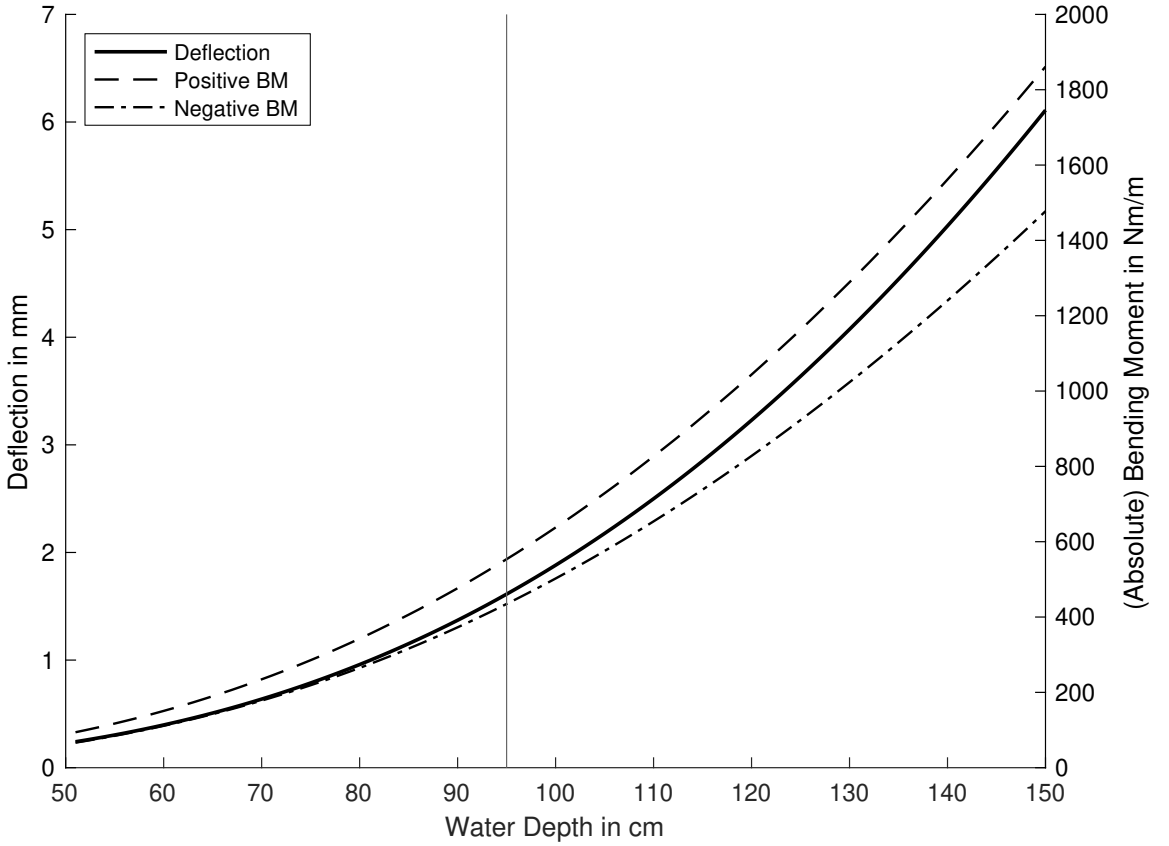

Figure 22. Maximum deflection, positive and negative (at supports) bending moments for various water depth values.

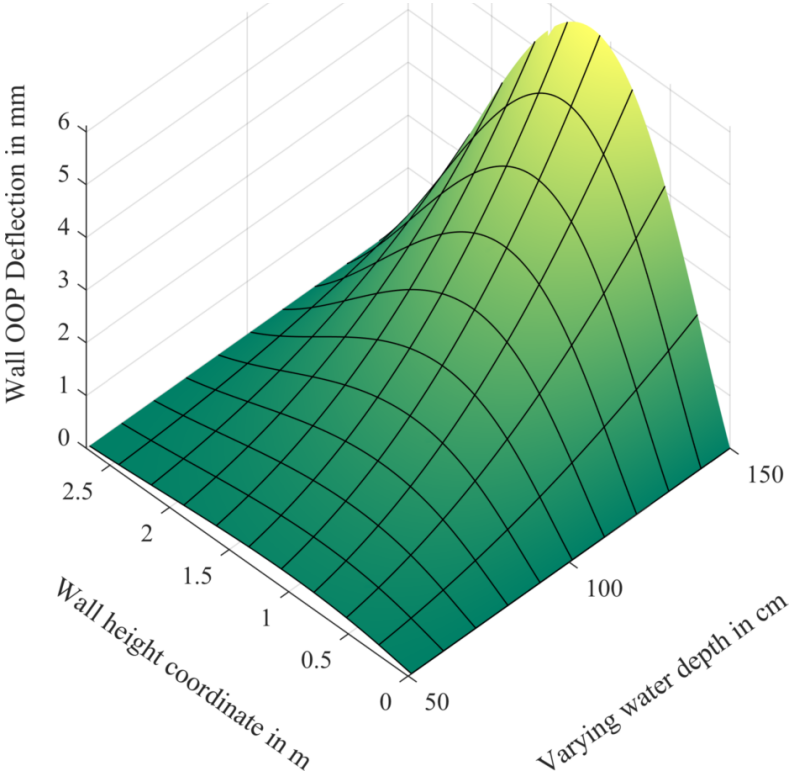

Figure 23. Out-of-plane deflection of the wall over its entire height (0 to 2.7m) for one-way bending under increasing water depth (50 to 150 cm).

The capacity of the wall in a one way configuration can be computed with the following equation:

$$M_R = \left(f_{x_1} + \sigma_{vert}\right) \cdot \frac{t^2}{6} \qquad \text{Equation 1}$$

$$\frac{M_S}{\sigma_{vert} \cdot t} \leq \frac{t}{2} \qquad \text{Equation 2}$$

where M_R is the resistive moment (capacity), f_{x1} is the flexural strength in the vertical direction σ_{vert} is the vertical compressive stress, t is the thickness of the wall, and M_S is the solicitations bending moment. Equation 2 corresponds to the stability criterion of the wall which assumes that the wall is fully cracked and cannot withstand any tensile (bending) stress; this is a conservative assumption used for design. A virgin wall, however, will resist some tensile stress.

For a bending strength of 300 kPa and a vertical stress of 50 kPa, the moment capacity of the wall is computed around 590 Nm/m, which corresponds, according to Figure 22, to about 95 cm of water depth. Table 5 presents a few combinations from a sensitivity study computed with the analytical model.

Table 5. Sensitivity of the most relevant model parameters for model A.

Rotational stiffness	Flexural strength (fx1)	Failure Water Depth
∞	200 kPa	69 cm
∞	300 kPa	78 cm
∞	400 kPa	86 cm
250 kN/rad	200 kPa	86 cm
250 kN/rad	**300 kPa**	**97 cm**
250 kN/rad	400 kPa	106 cm
0 N/rad	200 kPa	68 cm
0 N/rad	300 kPa	78 cm
0 N/rad	400 kPa	85 cm

3.2. Finite Element Model (B)

Additional models use the finite element method, where the wall is subdivided into small sections or rectangles connected via nodes. Both linear and non-linear FE models have a similar configuration with the exception that the non-linear models employ a non-linear material model for the wall; in both cases the material model is isotropic and follows the continuum approach. All FE models, as illustrated in Figure 24, are simply supported on all three directions at the bottom and on both horizontal directions at the top. Furthermore, a rotational spring, which limits the in-plane rotation at both top and bottom boundaries, is included in the models to consider the influence of the steel beams which provide some rotational restraint. Additionally, both lateral boundaries are connected to a boundary interface which limits the horizontal deformation perpendicular to the wall. The stiffness of this interface is zero for the one-way bending models, and 35 MN/m^3 for the two-way bending models representing the flexibility of the timber supports. A line load, mimicking the weight of the steel beam and the applied vertical stress, is included at the top, while, on the face of the wall, a triangular, hydrostatic pressure is applied, as depicted on the right of Figure 24. This illustration also shows the mesh of the model with 27x27 elements of 100mm by 100mm. The basic properties of the models are shown earlier in Table 4.

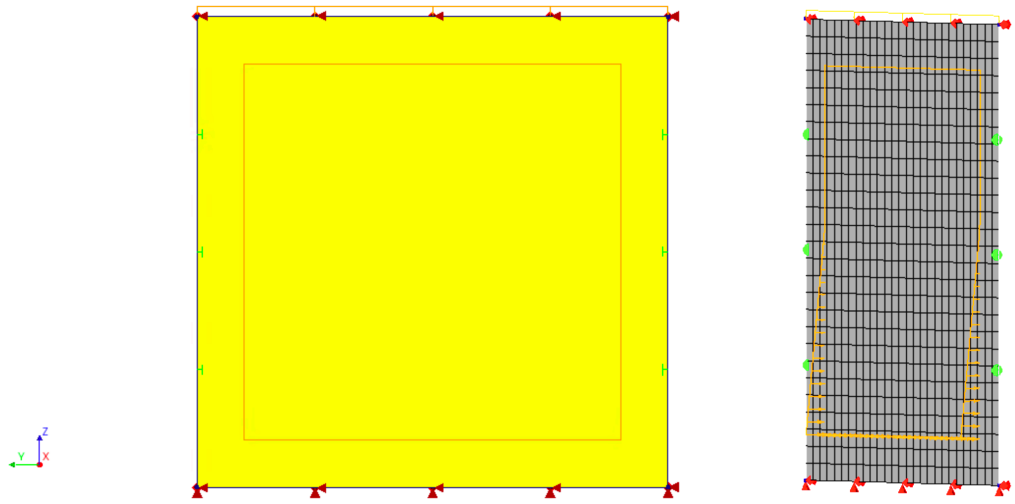

Figure 24. Boundaries and loads for the finite element models. Right, 3D view in perspective to show perpendicular hydrostatic pressure.

For the linear-elastic model discussed in this section (Model B), the bending moment distribution as a result of the load can be compared to the capacity of the wall computed separately. The vertical flexural strength of masonry (f_{x1}) and the horizontal flexural strength (f_{x2}) can be used to determine the bending capacity in each direction. For the vertical case, the overburden stress can be added as a beneficial effect. These are presented in Table 6. The capacity for bending in the horizontal direction is greater; this is explained because the bricks have to be twisted against each other whereas for the vertical direction, the mortar joints are bent open, an easier damaging action. However, the bending moment that develops due to the load applied to the wall is larger in the vertical direction due to the nature of the load and the boundaries; this is depicted in Figure 25 where the bending moment distribution for both vertical and horizontal directions is compared. Moreover, this effect is also observed in Table 6, and it is clear that already at 90 cm of water level in front of the wall (and no water behind the wall), the capacity for bending in the vertical direction is exceeded at the middle of the wall. To also reach the horizontal capacity, the water level has to increase above 140 cm. The linear-elastic model is incapable of considering the redistribution of the stresses that occurs when the vertical capacity is exceeded; as an area of the wall cracks, the cracks propagate and the pressure of the water is redistributed to be resisted in the horizontal direction. This means that the linear model can be used to estimate the capacity of the wall in terms of water depth with a large margin between 90 and 150 cm. A more accurate interval can only be obtained with a non-linear model.

Nevertheless, up to the water depth of 90 cm, where the wall is expected to remain elastic, the linear-elastic model, considering two-way bending, can be used to estimate the deformations of the wall. At 90 cm the

model predicts a deformation of about 0.6 millimetres which corresponds well with the experimental results. Yet, for higher water levels, the model indicates unrealistically low deformations, a fact attributable to its lack of nonlinearity.

Table 6. Maximum bending moment for various water levels.

Water Level (cm)	Model B	
	Vertical	Horizontal
Capacity	**590 Nm/m**	**840 Nm/m**
90	640 Nm/m	230 Nm/m
120	1,250 Nm/m	520 Nm/m
130	1,490 Nm/m	645 Nm/m
140	1,760 Nm/m	785 Nm/m

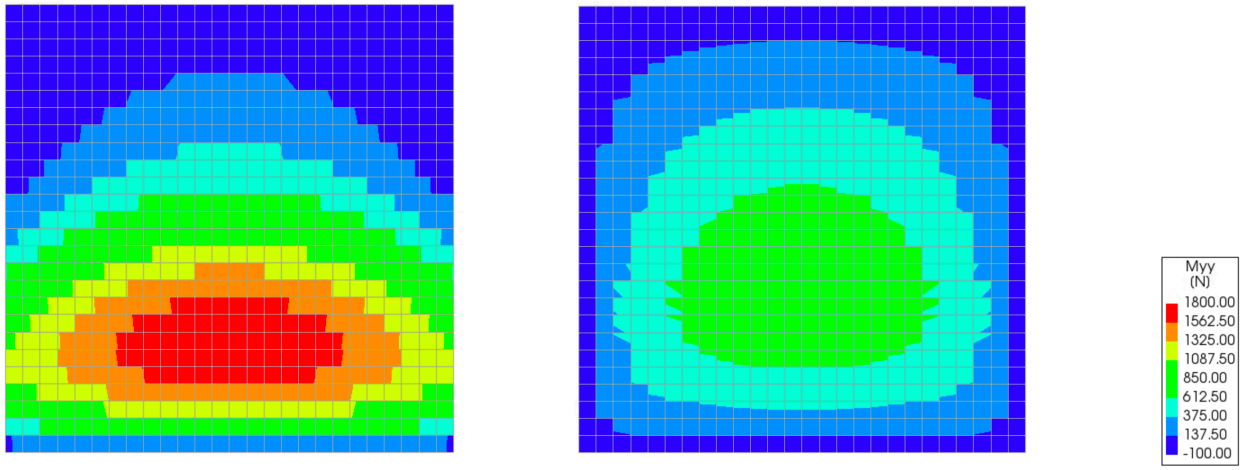

Figure 25. Bending moment distributions for vertical (left) and horizontal (right) bending. Values are expressed in the same scale and in Nm per metre stretch for the case of 140 cm of water.

3.3. Non-Linear Finite Element Models

All subsequent models were made using a non-linear material model for the masonry. This means that the model is capable of developing cracks once the masonry tensile strength is reached somewhere in the model. The Total Strain Rotating Crack (TSRC) model was employed due to its suitability for shell elements. The Engineering Masonry Model (EMM), which offers some advantages over the TSRC for masonry, was not used because the EMM requires a larger number of material parameters and the TSRC is better suited for out-of-plane cracking in shell elements. Moreover, the comparison models with EMM were slower to run and presented larger deformation with smaller crack widths, neither of which corresponded better to the experimental data.

3.3.1. One-Way Bending (Model C)

The first non-linear model was run simulating the case of one-way bending where the lateral constraints of the wall are not effective. Already at 100 cm of water depth, the model suddenly displayed large deformations as shown in Figure 26; any deformation above 50 mm can be reasonably linked to the failure of the wall.

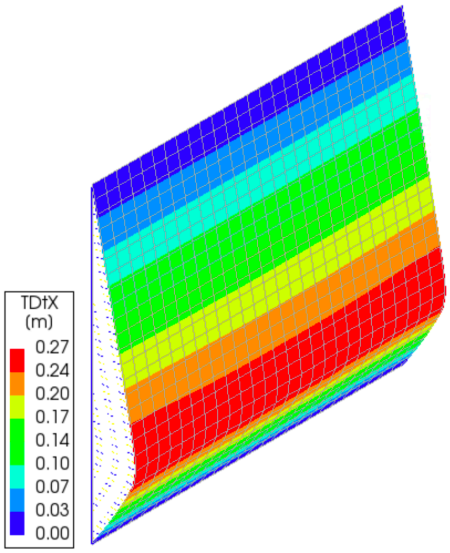

Figure 26. Model without lateral constraints, showing very large out-of-plane deformation of 270mm at 100 cm of water depth, essentially indicating failure.

3.3.2. Two-Way Bending (Model D)

An identical model but employing an interface at the sides between the wall and the two steel columns causes the wall to bend in both directions. The interface doesn't provide any rotational stiffness and is thus limited to a translational stiffness in the direction perpendicular to the plane of the wall. This stiffness was calibrated to mimic the restraint provided by the timber profile placed at the edges of the wall and fastened to the steel columns. Figure 27 depicts the deformation and crack pattern obtained with this model at a water depth of 130 cm. The model indicates that the wall deforms about 10 mm out of plane and develops a horizontal crack with an opening of up to 3 mm around the bottom third of the wall. Increasing the water depth by 10 cm leads to a large increase in deformation as is shown in Figure 28. Here, a water depth of 140 cm leads to wider cracks of up to 5.5 mm and an almost 60% larger deformation of 16 mm.

In terms of sensitivity, the most influential parameter in a non-linear model is the tensile strength of the masonry. In this case, a relatively high value for old masonry was chosen (150 kPa) since the wall was built with a bit more water to compensate building conditions. However, if the value is set to 100 kPa in the model, then the expected maximum deflection increases from 6.5 to 8.5 mm, a 30% increase for a 33%

reduction. This is a fair relationship between input and output and emphasises the use of well-monitored material properties and probabilistic parameters in (non-linear) models.

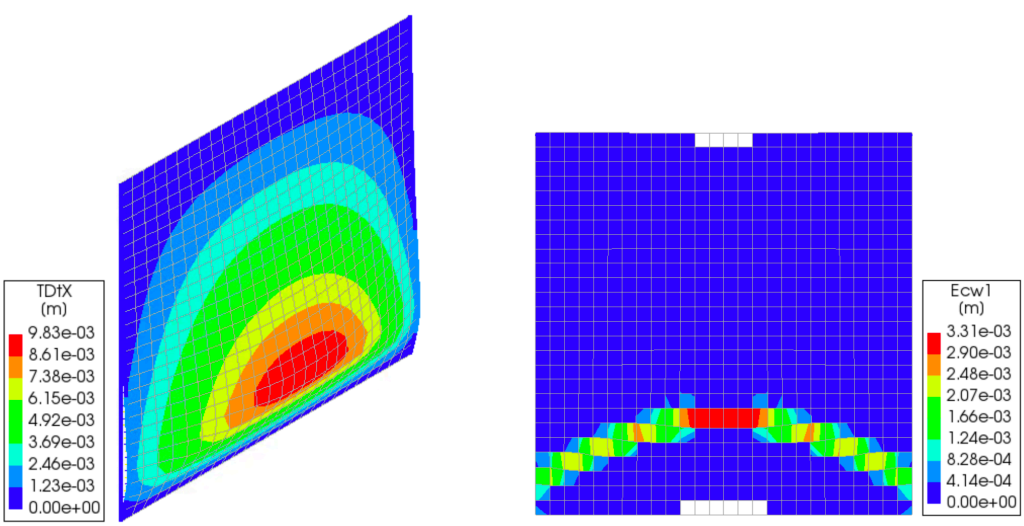

Figure 27. Two-way bending at a water depth of 130 cm.

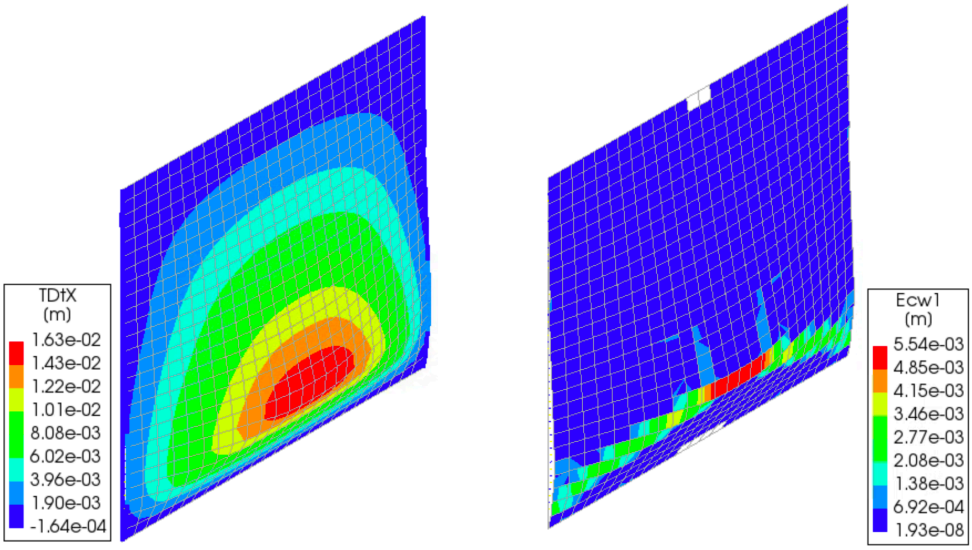

Figure 28. Two-way bending at a water depth of 140 cm.

3.4. Comparison Hydrostatic Pressure

A first comparison can be drawn between the finite-element models mentioned hereto. Both linear and non-linear two-way bending models (B and D) output similar deformation values up to a water depth of 90 cm, corresponding to the linear behaviour of the wall. This is verified by Model C, which bends only one-way and can thus not rely on the redistribution of the stresses and indicates failure just above 90 cm. This comparison is summarised in Table 7. Here, it can be observed how the linear model outputs unrealistically low deformations for high water depths. Conversely, the non-linear model displays increasing deformation up to a loading level where the wall starts to develop cracks. Then, the rate of increase of the out-of-plane deformation also increases until shortly after a water depth of 140 cm when failure occurs. This progression is compared to the experimental data in Figure 29. The sensor values for the three sensors are averaged for the first two tests, and the mean between both tests is also depicted. The three sensors form a triangle around the point of maximum deflection (according to the model), while the model data corresponds to the maximum deflection. In this light, it is expected that the mean sensor values are slightly lower than the model data. The first two tests are contrasted because they correspond to the most virgin condition of the wall and also attained the highest water levels. The experimental data is fitted to a power model of the form $[a \cdot x^b + c]$ and drawn on a logarithmic scale. Note that in the latter case the data is shifted horizontally so that the line crosses the origin. Both curves suggest that there is a linear region up to where the deformation increases slowly and which is followed by a region where the deformation increases faster at rising water depth. The values obtained from the non-linear models show a similar yet more intensely contrasted linear and non-linear regions. Due to the sharp increase in deformation when cracking is predicted, the model lies stiffer up to 110 cm and more flexible from 110 cm upwards compared to the experimental data. This was deemed a reasonable compromise as the water level, at which significant cracking leads to larger deformation, is sensitive to boundaries of the model and the material parameters implemented herein.

The comparison figure also includes the analytical model (A), which, because of its one-way bending, appears more flexible than the two-way models. Nevertheless, the trend represented by the analytical model agrees well with the experimental data until 110 cm approximately when cracking becomes important. In fact, model A describes the perfect linear-elastic behaviour which is displayed in this logarithmic graph as an upward curvature. Both experimental data fits display a similar curvature, but unlike the analytical model, the curvature reverses over an inflection point located at about 90 cm of water depth. It is clear, hence, that at 90 cm of water depth the wall starts to develop micro cracks and a redistribution of stress between the vertical and horizontal directions takes place; then, at a hydrostatic load 20 cm greater, crack patterns start to fully develop which leads to a large increase in the out-of-plane deformation.

Table 7. Comparison between various models.

Water Level (cm)	Model B	Model C	Model D	
	Displacement		Displacement	Crack Width
90	0.6 mm	2.4 mm	0.7 mm	0 mm
100	n.d.	500 mm	1 mm	0 mm
110		n.a.	1.5 mm	< 1 µm
120			7 mm	2.7 mm
130			9.8 mm	3 mm
140	2 mm		16 mm	5.5 mm
150	2.4 mm		500 mm	n.a.

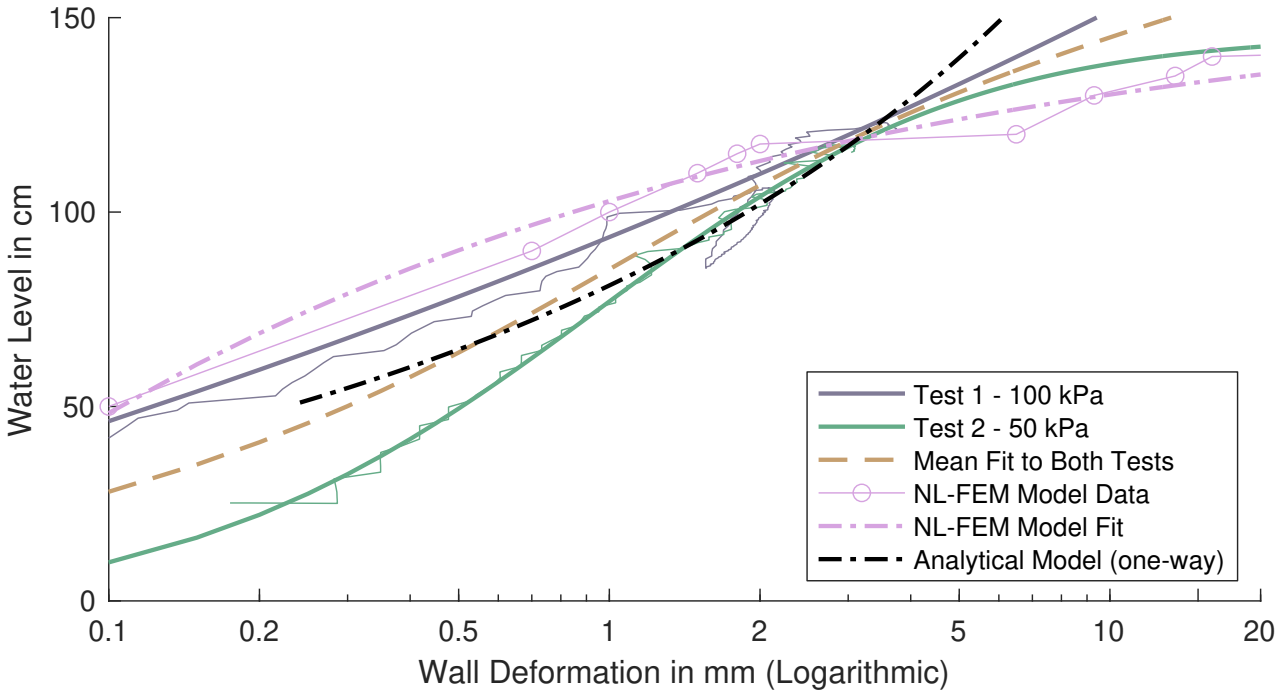

Figure 29. Comparison between Model D and experimental data.

The experiments and the models reveal that the wall was always restrained in two directions, ergo, from all four boundaries. Even when the timber restraints where removed, the wall continued being attached to the side columns. The masonry had been placed flush with the columns but had not been attached to the steel in any way; only a silicone sealant was used to prevent water seeping at the sides. This sealant does not have the capacity to support the masonry, especially with the forces capable of shifting the testing rig backwards. Consequently, a different effect must be responsible for the support of the wall at the sides and the failure to achieve both two- and one-way bending in the experiment. One hypothesis is that the pressure of the water on the side of the testing rig exerted a horizontally-compressive force on the masonry and that this force, together with the friction between steel and masonry managed to affix the sides of the wall in place. However, a modified non-linear model, where the side interfaces where made non-linear to include friction, reveals that the lateral force would have had to be much higher than what the entire pressure on the side of the setup could generate. Another explanation lays in the shifting of the frame. Figure 16 illustrates how the testing rig was displaced due to the hydrostatic pressure; this displacement could be linked to a mechanism that grasped the masonry in place. Furthermore, the hygro/thermal expansion and contraction of the frame together with that of the masonry could play a role even if the expansion coefficient of steel is higher than that of masonry and the testing period was noticeable warmer than the construction period. Finally, the out-of-plane deflection causes an horizontal arching phenomenon in the wall which adds a horizontally-compressive force; however, this confining force needs to be countered and there are no rigid elements to provide such confinement. All in all, future wall tests should incorporate a five millimetre rubber seal to prevent the masonry becoming fixed to the steel frame at the side boundaries.

3.5. Models With Debris

The experiments with debris are presented separately since they are more difficult to compare than the simple hydrostatic pressure. As can be seen in Figure 14, the impact of (hard) debris led to large jumps in out-of-plane deformation of 1 up to 8 mm, reaching ultimate deformation values of about 17 mm before local failure of the masonry rendered the collisions ineffective.

To also account for the fact that the wall had sustained damage at the time of debris testing, a phased approach is implemented using the non-linear, two-way bending model (Model D); see section 3.3.2. First, the wall is loaded with a water depth of 130 cm and subsequently unloaded. This leads to a residual deformation and cracked integration points. Then, a water depth of 100 cm is applied producing a deformation of 4.1 mm, significantly larger than the 1 mm predicted by the model on a virgin wall (see Table 7). Then, the load equivalent to the impact of the debris is applied two times. This load, however, requires some discussion. Since the case of the tree log did not lead to noteworthy results, only the case of the hard debris is modelled. The impact is converted into a distributed force over a square of 30 x 30 cm placed just above the water line. The kinetic energy is transformed into potential elastic energy, where the stiffness of the impact (k) plays a role. The stiffness of the wall (k_w) for such a point load can be computed by applying a unitary load and determining the displacement; this results in a value of 4.5 MN/m. Next, since the stiffness of the steel cube (k_d) in regards to its centre of gravity is very large and much larger than that of the wall, it can be assumed to be infinite and thus only the stiffness of the wall is taken into account. Consequently, the impact pressure follows the equation:

$$q = \frac{v \cdot \sqrt{m \cdot k}}{A} \qquad \text{Equation 3}$$

where v is the velocity of the debris, m is the mass of the debris, k is the total stiffness of the impact (note that to combine stiffnesses the inverse sum is used), and A is the area over which the collision is distributed. Figure 30 depicts the case of an object of mass of 1800 kg colliding with the wall at 1 m/s; this is the largest impact that the wall could sustain simultaneously with 100 cm of water depth, determined from several model iterations. It is to note that the crack pattern resembles that observed during the debris tests; also the beginning of diagonal cracks travelling upwards from the centre of the wall is to be observed. Table 8 provides a summary of some interesting model results.

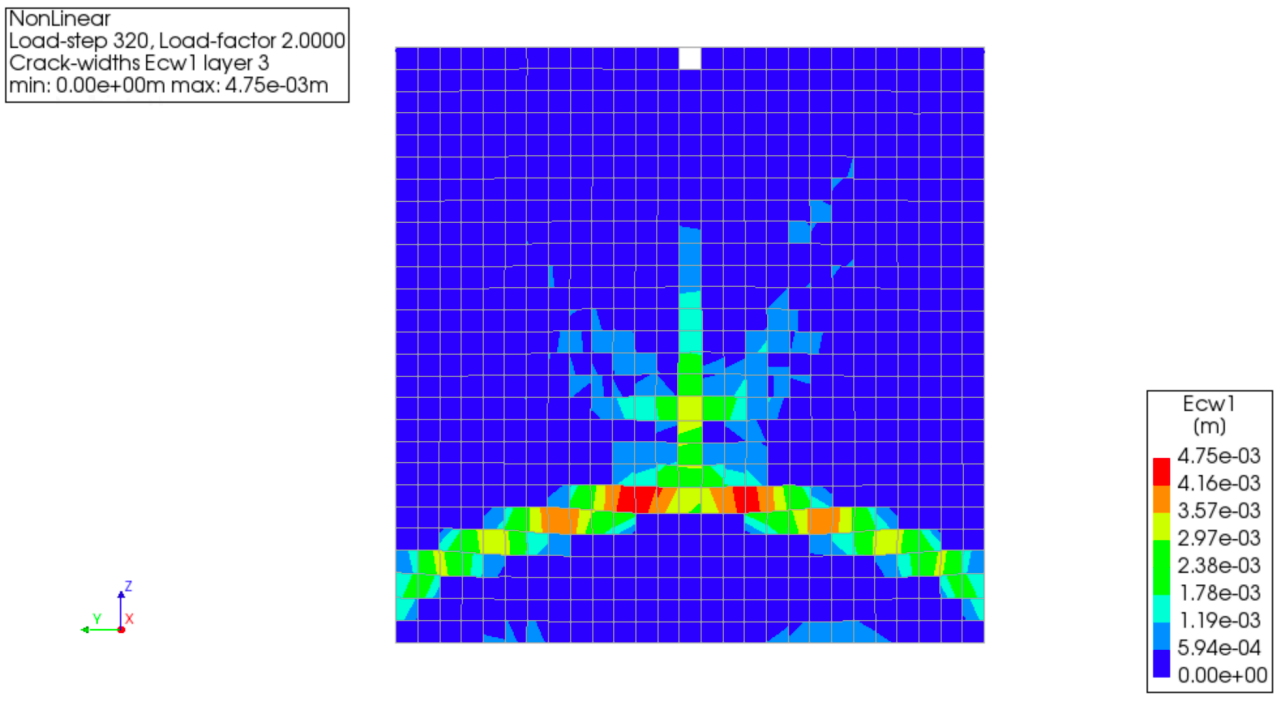

Figure 30. Debris collision on pre-damaged masonry wall (at 130 cm waterdepth) simultaneous with 100 cm of water depth using Model D. The point of impact is identifiable by the cross-like crack pattern.

Table 8. Examples of maximum deformation reached for debris collisions.

Velocity	Mass	Deformation	Stiffness (k_d)	Notes
3 m/s	40 kg	8.4 mm	∞	Steel Cube
3 m/s	60 kg	10 mm	∞	
3 m/s	80 kg	11.5 mm	∞	
3 m/s	100 kg	13 mm	∞	
1 m/s	1,800 kg	22.7 mm	∞	Steel Boat (not tested)
1 m/s	2,000 kg	710 mm	∞	
1 m/s	80 kg	5.8 mm	94 MN/m	Tree Log

One point to note from these calculations is that the impact force was determined using the elastic stiffness of the wall (k_w) while in reality, especially after a first collision, the damaged stiffness corresponding to the already-cracked wall, would be lower and more applicable. This would lead to a lower force, however, which makes the presented models more conservative. Nonetheless, the damaged wall could also be more vulnerable when exposed to debris loads, hence, these results should be considered with a high uncertainty.

4. Conclusions and Future Tests

4.1. Limitations

It is important to view the experiment presented herein, and the conclusions derived from it, within its limitations. No experiment can represent reality perfectly, especially when the intrinsic variability in the real world renders a single experiment insufficient to depict all potential cases, as is the case of one wall subjected to hydrostatic pressure. Nevertheless, the configuration of the wall in this report was made as universal as possible so as to draw the most significant conclusions in the situations where understanding was most lacking. First, the material of the wall, fired-clay brick masonry, corresponds to that employed for the outer veneer of the majority of Dutch houses, 70% of which sport a cavity wall [1]. Yet, other materials are also used and the degree to which they behave similarly to the tested wall will depend on their material properties. Furthermore, even similar materials will vary in strength due to construction and ageing effects. Besides, the failure of the outer veneer does not necessarily lead to the failure of the structure. Secondly, for the structures where the load-bearing wall is built of similar masonry to that tested here (about 10%), the boundary conditions and dimensions of the walls are diverse. The wall tested herein represents the most common boundaries, where some restraint is provided by the floors and lateral walls; however, the square dimensions of the wall are mostly to investigate the effect of the lateral boundaries. Wider walls will benefit less from this effect, and as a consequence, their behaviour necessitates less study. Thirdly, the effect of openings and the interaction between the two leaves in a cavity wall are conditions which will affect the behaviour of the wall tested, but that could not be included in this experiment.

4.2. Conclusions

Loading of a one-hundred-millimetres-thick masonry wall using water to produce a true hydrostatic pressure reveals that a small deflection of a few millimetres can be expected before a non-linear, rapid increase of this out-of-plane deformation occurs. The large deflection reaches values of approximately 20 mm before ultimately leading to wall collapse, determined by a simulation. A water depth of about 90 cm corresponds to be beginning of masonry damage, with about 2 mm deflection, measured experimentally and reproduced numerically. The damage, consisting of cracks, propagates as the water depth increases. At a water depth of 140 cm, which could not be reached experimentally, the validated numerical models predict the collapse of the wall.

Hence, it can be concluded that a traditional masonry wall, with a thickness of at least 0.1m and restrained at its top boundary, will resist a hydrostatic pressure equivalent to a water depth of 0.9 metres even if there is no water depth present behind the wall and especially if the wall is constrained at its sides. In the latter case, a wall with an aspect ratio of 1:1 could withstand up to 1.40 m. The masonry does not experience important leakage even after a few hours of sustained water pressure; only wetness is observed at the inner side.

An analytical model of the wall is sufficiently accurate to model the deformation and capacity of the wall in cases where the wall is more than twice as wide as it is tall or is not support at its side; i.e. the wall is modelled in two dimensions and in one-way bending. For the square wall tested, such a model was not adequate; a two-way bending model was necessary to mimic the deformation of the masonry wall. Yet, for a correct representation of the wall's deflection beyond 60% of its capacity expressed as water depth, a non-linear two-way bending model is required, as the cracking masonry cannot simply be modelled linear-elastically. In other words, to properly model a masonry wall subjected to hydrostatic pressure, a three-dimensional model employing a non-linear material model tailored to masonry behaviour is required.

The experiments detailed herein and the calibrated models derived from them can be used in a future extrapolation study to explore a large variety of situations beyond the objective of this report. While chapter three focused on replicating the experimental results with a modelling approach that rendered reasonable results, an extrapolation study could use this validated approach to determine the behaviour and the failure conditions of wider, narrower, thicker, better connected, or stronger walls at higher or lower

water levels, with debris impact at different velocities and angles, stiffness and mass. This information could prove invaluable in a myriad of scenarios linked to the analysis of the fragility of dutch buildings.

4.3. Future Tests

Future tests should improve the watertightness of the testing rig and fix the piping issues discovered in this first wall test. Additionally, the edges of the masonry should be well separated from the steel frame in a way that allows a restraint that can be activated and disconnected on demand so as to also explore one-way bending.

Moreover, potential future tests could investigate:

- a wall built of calcium-silicate bricks which are more porous and constitute a stiffer and stronger masonry.
- a cavity wall comprising two masonry leaves connected with ties; the water level inside the cavity could be measured. Also, gaps in the inner leaf would allow the instrumentation to be installed, albeit above the maximum water level.
- a wall/cavity wall with a window frame. The window would be built with a timber frame and connected with old-fashioned sealants to investigate leakage and the weakening effect of an opening in the masonry wall.

4.4. Acknowledgements

The authors would like to acknowledge the assistance of various institutions and persons who helped realise these experiments.

First, BSc-student Serban Alexandru, who helped immensely in the physical preparation of the experiments by working in the polder. The experiment wouldn't have come to fruition without the coordination of dr. Jeremy Bricker, the input from dr. Andrés Diaz-Loaiza and the discussions with prof. Bas Jonkman, dr. Karin de Bruijn from Deltares, dr. Bas Kolen from HKV, and ir. Durk Riedstra from WVL.

Furthermore, the experiments conducted at Flood Proof Holland are in debt to Lindsey Schwidder from the VP Delta - TU Delft union for the possibility to test there.

References & Further Reading

1. Arub Exposure Database EDB V5 Structural Systems (2018) - Groningen Building Taxonomy analysis
2. S. Jafari, R. Esposito, J.G. Rots, F. Messali (2017). Characterizing the Material Properties of Dutch Unreinforced Masonry. Procedia engineering, 193, 250-257
3. M. Damiola, R. Esposito, F. Messali, J.G. Rots (2018). Quasi-Static Cyclic Two-Way Out-Of-Plane Bending Tests And Analytical Models Comparison For URM Walls. 10th International Masonry Conference, Milan
4. Korswagen, P.A. (2016). Structural Damage to Masonry Housing due to Earthquake-Flood Multi-hazards - A framework to assess damage from earthquakes and floods, together with a case study in the province of Groningen in the Netherlands. MSc Thesis. Delft University of Technology
   http://resolver.tudelft.nl/uuid:26b0b336-527a-43a8-a98f-9cc7555765e7
5. L. Jansen, P.A. Korswagen, J.D. Bricker, S. Pasterkamp, K.M. de Bruijn, S.N. Jonkman (2020). Experimental determination of pressure coefficients for flood loading of walls of Dutch terraced houses. Engineering Structures 216 (2020) 110647
   doi.org/10.1016/j.engstruct.2020.110647
6. Bratz, B. (2019). Hydrodynamic Loading of Dutch terraced houses due to flood actions using Computational Fluid Dynamics. MSc Thesis. Delft University of Technology
   http://resolver.tudelft.nl/uuid:255c83b1-ccbc-494a-8784-7fc3474e4bff
7. Brussee, A. (2020). Improving flood fatality risk assessment for river flooding in the Netherlands. MSc Thesis. Delft University of Technology.
   http://resolver.tudelft.nl/uuid:2d1b99f0-7d9c-423a-b2f0-cb11b563a00a

Appendixes

Appendix A - Equivalent Bending Moment

To estimate the severity of the loading when water is present behind the wall, an equivalent solicitations bending moment is determined. Note that this bending moment does not necessarily correlate to the internal bending moment that develops in the wall; this is more accurately calculated in Appendix B.

Following the scheme presented in Figure A.1: Firstly, the pressure applied to the the wall as a result of a water depth in front and behind the wall is schematised. Secondly, the distributed, triangular pressure is approximated to a point load located at two-thirds the depth measured from the surface of the water. Each point load produces a known, linear bending moment as depicted in the third box. Fourthly, under the principle of linear superposition, the two bending moment lines can be subtracted to produce an equivalent bending moment line from where the maximum equivalent bending moment can be observed.

It must be emphasised that this is an approximation since the hydrostatic pressure leads to a more complex moment line than depicted here; yet, due to the sensitivity of the model boundaries and other parameters, this approximation is a reasonable estimation of the severity of the load when water is present both in front and behind the wall.

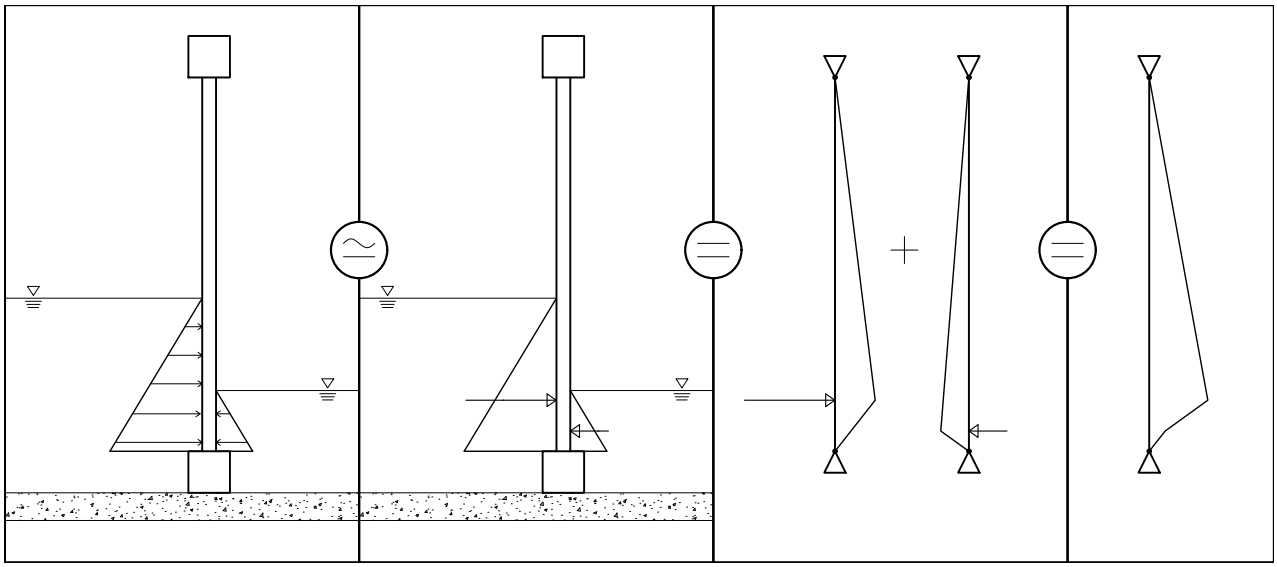

Figure A.1. Equivalent bending moment from water levels.

Appendix B - Analytical Solution Model A

General Equations

```
> restart :
> w4 := diff(w(x), x$4) = -(-q0·a + q0·a·x / a);
```

$$w4 := \frac{d^4}{dx^4} w(x) = q0\,a - q0\,x \tag{1.1}$$

```
> w0 := dsolve(w4) :
> w0; diff(w0, x); diff(w0, x$2); diff(w0, x$3); diff(w0, x$4);
```

$$w(x) = -\frac{1}{120} q0\,x^5 + \frac{1}{24} q0\,a\,x^4 + \frac{1}{6} \_C1\,x^3 + \frac{1}{2} \_C2\,x^2 + \_C3\,x + \_C4$$

$$\frac{d}{dx} w(x) = -\frac{1}{24} q0\,x^4 + \frac{1}{6} q0\,a\,x^3 + \frac{1}{2} \_C1\,x^2 + \_C2\,x + \_C3$$

$$\frac{d^2}{dx^2} w(x) = -\frac{1}{6} q0\,x^3 + \frac{1}{2} q0\,a\,x^2 + \_C1\,x + \_C2$$

$$\frac{d^3}{dx^3} w(x) = -\frac{1}{2} q0\,x^2 + q0\,a\,x + \_C1$$

$$\frac{d^4}{dx^4} w(x) = q0\,a - q0\,x \tag{1.2}$$

```
> v4 := diff(v(x), x$4) = 0;
```

$$v4 := \frac{d^4}{dx^4} v(x) = 0 \tag{1.3}$$

```
> v0 := dsolve(v4) : v0 := v(x) = 1/6 _c1 x^3 + 1/2 _c2 x^2 + _c3 x + _c4 :
> v0; diff(v0, x); diff(v0, x$2); diff(v0, x$3); diff(v0, x$4);
```

$$v(x) = \frac{1}{6} \_c1\,x^3 + \frac{1}{2} \_c2\,x^2 + \_c3\,x + \_c4$$

$$\frac{d}{dx} v(x) = \frac{1}{2} \_c1\,x^2 + \_c2\,x + \_c3$$

$$\frac{d^2}{dx^2} v(x) = \_c1\,x + \_c2$$

$$\frac{d^3}{dx^3} v(x) = \_c1$$

$$\frac{d^4}{dx^4} v(x) = 0 \tag{1.4}$$

Requisite Equations

Boundary conditions for the bottom section:
1) bottom displacement is zero
w(0) = 0
2) rotation times rotational stiffness equals the bending moment at bottom
w'(0)·ka=M=EI·w"(0)

```
> eq1 := 0 = subs(x = 0, rhs(w0));
```

$$eq1 := 0 = \_C4 \tag{2.1}$$

```
> eq2 := subs(x = 0, rhs(diff(w0, x$1)))·ka = ei·subs(x = 0, rhs(diff(w0, x$2)));
```

$$eq2 := \_C3\,ka = ei\,\_C2 \tag{2.2}$$

Boundary conditions for the top section:
1) top displacement is zero
v(a+b) = 0
2) rotation times rotational stiffness equals the bending moment at top
v'(a+b)·kc = M = EI·v"(a+b)

```
> eq3 := subs(x = a + b, rhs(diff(v0, x$1)))·kc = -ei·subs(x = a + b, rhs(diff(v0, x$2)));
```

$$eq3 := \left(\frac{\_c1\,(a+b)^2}{2} + \_c2\,(a+b) + \_c3\right) kc = -ei\,(\_c1\,(a+b) + \_c2) \tag{2.3}$$

```
> eq4 := subs(x = a + b, rhs(v0)) = 0;
```

$$eq4 := \frac{\_c1\,(a+b)^3}{6} + \frac{\_c2\,(a+b)^2}{2} + \_c3\,(a+b) + \_c4 = 0 \tag{2.4}$$

Compatibility conditions at the middle:
Equal displacement

```
> comp1 := subs(x = a, rhs(w0)) = subs(x = a, rhs(v0));
```

$$comp1 := \frac{1}{30} q0\,a^5 + \frac{1}{6} \_C1\,a^3 + \frac{1}{2} \_C2\,a^2 + \_C3\,a + \_C4 = \frac{1}{6} \_c1\,a^3 + \frac{1}{2} \_c2\,a^2 + \_c3\,a + \_c4 \tag{2.5}$$

Equal rotation

```
> comp2 := subs(x = a, rhs(diff(w0, x$1))) = subs(x = a, rhs(diff(v0, x$1)));
```

$$comp2 := \frac{1}{8}\,q0\,a^4 + \frac{1}{2}\,\_C1\,a^2 + \_C2\,a + \_C3 = \frac{1}{2}\,\_c1\,a^2 + \_c2\,a + \_c3 \tag{2.6}$$

Equal bending moment

```
> comp3 := subs(x = a, rhs(diff(w0, x$2))) = subs(x = a, rhs(diff(v0, x$2)));
```

$$comp3 := \frac{1}{3}\,q0\,a^3 + \_C1\,a + \_C2 = \_c1\,a + \_c2 \tag{2.7}$$

Equal shear force

```
> comp4 := subs(x = a, rhs(diff(w0, x$3))) = subs(x = a, rhs(diff(v0, x$3)));
```

$$comp4 := \frac{q0\,a^2}{2} + \_C1 = \_c1 \tag{2.8}$$

Equal load (verification)

```
> comp5 := subs(x = a, rhs(diff(w0, x$4))) = 0;
```

$$comp5 := 0 = 0 \tag{2.9}$$

▶ Parameters

▼ Solution

```
> solution := solve({eq1, eq2, eq3, eq4, comp1, comp2, comp3, comp4}, {_C1, _C2, _C3, _C4, _c1, _c2, _c3, _c4}) :
> wd0 := evalf(subs(a = waterheight, subs(a = waterheight, b = 2.7 − waterheight, ka = k_rot, kc = k_rot, ei = EI, solution[1..4]),
      rhs(w0)));
```

$$wd0 := -81.75000000\,x^5 + 408.7500000\,x^4 - 737.9978192\,x^3 + 309.7207146\,x^2 + 412.9609530\,x \tag{4.1}$$

```
> vd0 := evalf(subs(a = waterheight, subs(a = waterheight, b = 2.7 − waterheight, ka = k_rot, kc = k_rot, ei = EI, solution[5..8]),
      rhs(v0)));
```

$$vd0 := 79.50218043\,x^3 - 507.7792855\,x^2 + 821.7109531\,x - 81.75000000 \tag{4.2}$$

```
> W := piecewise(x < 0, 0, x < waterheight, wd0/(0.001·EI), x > waterheight, vd0/(0.001·EI), x > 2.7, 0);
```

$$W := \begin{cases} 0 & x < 0 \\ -0.4904999999\,x^5 + 2.452500000\,x^4 - 4.427986914\,x^3 + 1.858324287\,x^2 + 2.477765718\,x & x < 1 \\ 0.4770130825\,x^3 - 3.046675712\,x^2 + 4.930265718\,x - 0.4904999999 & 1 < x \\ 0 & 2.7 < x \end{cases} \tag{4.3}$$

```
> Dplot := plot(W, x = 0..2.7, popts) :
>
```

▶ Rotation Angle

▶ Bending Moment

▶ Shear Force

▶ Summary

▶ Multiple Points

Appendix C - Sensor Specifications

Two sensors are used in the experiment presented herein: linear potentiometers employed as deflectometers and relative pressure sensors used as water depth sensors.

The pressure sensors and the potentiometers were attached to a data acquisition box that has two types of input: amplified (128 times) for wheatstone type sensors and direct voltage inputs with ratiometric analog to digital conversion (typically used with linear potentiometers). Both types are sampled with 24 bit precision at a rate of 1Hz. Further, the data acquisition box was connected digitally via USB to a PC running the MP3 software, proprietary to the Stevin Lab; the software sampled a data point every 60 seconds for every sensor (so configured) and registered it on a spreadsheet against time.

The software was calibrated for every sensor to account for their non-linearity and the voltage was converted into displacement in millimetres and pressure in centimetres of water column, respectively.

mm **13FLP**

Standard dimensions

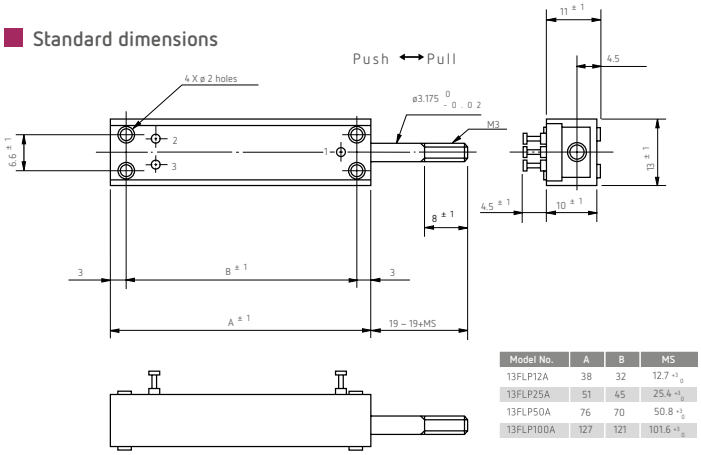

Model No.	A	B	MS
13FLP12A	38	32	12.7 +3 0
13FLP25A	51	45	25.4 +3 0
13FLP50A	76	70	50.8 +3 0
13FLP100A	127	121	101.6 +3 0

Model 13FLP25A

Model 13FLP100A

Standard Model Nos.

13FLP12A	stroke	12mm
13FLP25A	stroke	25mm
13FLP50A	stroke	50mm
13FLP100A	stroke	100mm

General Specifications

Model No.		13FLP12A	13FLP25A	13FLP50A	13FLP100A
Standard Resistance Values		500,1k,2k,5k,10k (Ω)	500,1k,2k,5k,10k (Ω)	1k,2k,5k,10k,20k (Ω)	1k,2k,5k,10k,20k (Ω)
Total Resistance Tolerance		±20% (K)			
Independent Linearity Tolerance	Standard Class	±2.0%	±1.5%	±1.0%	±0.7%
	Precision Class	±1.0%	±0.7%	±0.5%	±0.3%
Resolution		Essentially Infinite			
Output Smoothness		Within 0.1% against input voltage			
Contact Resistance Variation		Within 2% C.R.V.			
Power Rating		0.2W	0.4W	0.7W	1.2W
Electrical Stroke		12.7±0.5mm	25.4±0.5mm	50.8±0.5mm	101.6±0.5mm
Mechanical Stroke (MS)		12.7 +3 0 mm	25.4 +3 0 mm	50.8 +3 0 mm	101.6 +3 0 mm
Insulation Resistance		Over 1,000M Ω at 500V.D.C.			
Dielectric Strength		1 minute at 500 V.A.C.			
Friction		Within 0.5N (50gf)			Within 1.0N (100gf)
Stopper Strength		Approx. 20N (2kgf)			
Resistance Temperature Coefficient		±400p.p.m./°C			
Mass		Approx. 10g	Approx. 15g	Approx. 25g	Approx. 35g

Figure C.1. Data sheet of the linear potentiometers employed, 50 mm version.
https://www.althensensors.com/sensors/linear-position-sensors/linear-potentiometers/4882/13flp-series-linear-potentiometer/

The following three tables correspond to the relative pressure sensors, model 24PCXXH6D are were obtained from:

http://www.farnell.com/datasheets/2002508.pdf?_ga=2.217350869.2122701797.1601885315-1731703136.1594368064

Table 1. Absolute Maximum Ratings[1]

Characteristic	Min.	Typ.	Max.	Unit	Note
Supply voltage	2.5	10	12	Vdc	–
Input resistance	4	5	6	kOhm	–
Output resistance	4	5	6	kOhm	–
Time response	–	–	1	ms	2

[1]Absolute maximum ratings are the extreme limits the device will withstand without damage.

[2]Time required for the output to increase from 10% to 90% of span in response to a step change in input pressure from the specified min. to max. operating pressure.

Table 2. Technical Specifications

Characteristic	Parameter
Operating temperature range: without EPDM seals with EPDM seals	 -40 °C to 85 °C [-40 °F to 185 °F] -20 °C to 85 °C [-4 °F to 185 °F]
Storage temperature range	-55 °C to100 °C [-67 °F to 212 °F]
Soldering terminal temperature/time	315 °C [599 °F] max./10 s max.
Vibration	10 G at 20 Hz to 2000 Hz
Shock	100 G for 11 ms
Life	1 million cycles min.

Table 3. Performance Characteristics (Vcc =10.00 ±0.01 Vdc; Ta = 25 °C [77 °F])

Characteristic	Operating Pressure Range														Unit	Note
	0 psi to 0.5 psi		0 psi to 1 psi		0 psi to 5 psi		0 psi to 15 psi		0 psi to 30 psi		0 psi to 100 psi		0 psi to 250 psi			
	Typ.	Max.	Typ.	Max.	Typ.	Max.	Typ.	Max.	Typ.	Max.	Typ.	Max.	Typ.	Max.		
Span	–	35 ±10	–	45 ±15	–	115 ±30	–	225 ±60	–	330 ±90	–	225 ±69	–	212 ±68	mV	1
Null offset	–	0 ±30	–	0 ±30	–	0 ±30	–	0 ±30	–	0 ±30	–	0 ±30	–	0 ±30	mV	2
Linearity (Best Fit Straight Line, P2>P1)	±0.2	±1.0	±0.2	±1.0	±0.2	±1.0	±0.2	±1.0	±0.2	±1.0	±0.2	±1.0	±0.2	±1.0	%span	3
Null shift (0 °C to 25 °C, 25 °C to 50 °C)	±1.0	–	±1.0	–	±1.0	–	±1.0	–	±1.0	–	±1.0	–	±1.0	–	mV	4
Span shift (0 °C to 25 °C, 25 °C to 50 °C)	±5.0	–	±5.0	–	±5.0	–	±5.0	–	±5.0	–	±5.0	–	±5.0	–	%span	5
Repeatability and hysteresis	±0.5	–	±0.5	–	±0.5	–	±0.5	–	±0.5	–	±0.5	–	±0.5	–	mV	6
Overpressure	–	20	–	20	–	20	–	45	–	60	–	200	–	250	psi	7

[1]Span is the algebraic difference between the output signal measured at the upper and lower limits of the operating pressure range, where Port 2 (P2)>Port 1 (P1).

[2]The output signal obtained when zero pressure is applied to all available ports.

[3]The maximum deviation of product output from a straight line fitted to the output measured over the specified operating pressure range, calculated according to BFSL. The straight line is fitted along a set of points that minimizes the sum of the square of the deviations of each of the points ("least-squares" method).

[4]The maximum deviation in offset due to changes in temperature over the compensated temperature range, relative to offset measured at a reference temperature of 25 °C.

[5]The maximum deviation in span due to changes in temperature over the compensated temperature range, relative to full-scale span measured at a reference temperature of 25 °C.

[6]Repeatability is the maximum difference between the output readings when the same pressure is applied consecutively, under the same operating conditions, with pressure approaching from the same direction within the specified operating pressure range. Hysteresis is the maximum difference between output readings when the same pressure is applied consecutively, under the same operating conditions, with pressure approaching from opposite directions within the specified operating pressure range.

[7]Overpressure is the maximum pressure that may safely be applied to the product for it to remain in specification once pressure is returned to the operating pressure range. Exposure to higher pressures may cause permanent damage to the product. Unless otherwise specified, this applies to all available pressure ports at any temperature within the operating temperature range.

Figure 1. Circuit Diagram

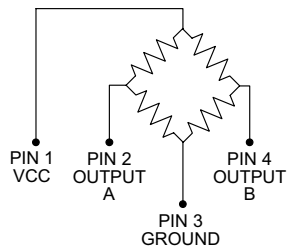

Output "A" increases as P2 pressure increases.

Output "B" deceases as P2 pressure increases.

Symbol	Description
Vcc	supply
OUTPUT A	bridge positive output
GROUND	ground
OUTPUT B	bridge negative output

Appendix D - Movies

Name	Description	Link
Test 1 - Back	Timelapse (20s) from the view of the back of the wall during the beginning of test 1.	edu.nl/keqbr
Test 1 - Back (2)	Timelapse (20s) from the view of the back of the wall during the second part of test 1.	edu.nl/qq337
Test 2 - Back	Timelapse (20s) from the view of the back of the wall during test 2.	edu.nl/ug3yf
Test 1 - Front - up to 110cm	Timelapse (20s) from the view of the front of the wall during the beginning of test 1 reaching a water level of 110 cm.	edu.nl/fx6pb
Test 1 - Front - up to 125cm	Idem, up to 125 cm.	edu.nl/atayp
Test 2 - Front	Timelapse (20s) from the view of the front of the wall during the beginning of test 2.	edu.nl/uypxt
Collection 1 - Soft Debris	A compilation of video clips showing the impacts of soft debris (tree log) against the front of the wall.	edu.nl/ue3hb
Collection 2 - Hard Debris	A compilation of video clips showing the impacts of hard debris (steel cube) against the front of the wall.	edu.nl/ffwv7